BIOCHEMISTRY

Small molecule OPA1 inhibitors amplify cytochrome c release and reverse cancer cells resistance to Bcl-2 inhibitors

Anna Pellattiero[1,2], Charlotte Quirin[1,2]†, Federico Magrin[1,2,3], Mattia Sturlese[4], Alberto Fracasso[3], Nikolaos Biris[5]‡, Stéphanie Herkenne[1,2]§, Laura Cendron[1], Evripidis Gavathiotis[5], Stefano Moro[4], Andrea Mattarei[3], Luca Scorrano[1,2]*

The guanosine triphosphatase (GTPase) activity of the mitochondrial dynamin-related protein Optic Atrophy 1 (OPA1) regulates cristae remodeling, cytochrome c release, and apoptosis. Elevated OPA1 levels in multiple cancers correlate with reduced therapy sensitivity and poor survival, calling for specific OPA1 GTPase inhibitors. A high-throughput screening of ~10,000 compounds identified MYLS22, a heterocyclic *N*-pyrazole derivative as a reversible, noncompetitive OPA1 GTPase inhibitor. MYLS22 engaged with OPA1 in vitro and in cells where it induced cristae remodeling and mitochondrial fragmentation contingent on intactness of its predicted OPA1 binding site. MYLS22 enhanced proapoptotic cytochrome c release and sensitized breast adenocarcinoma cells to anti–Bcl-2 therapy, without toxicity on noncancer cells. By MYLS22 structure-activity relationship studies, we obtained Opa1 inhibitor 0 (Opitor-0) that inhibited OPA1, promoted cytochrome c release, and restored anti–Bcl-2 therapy sensitivity more efficiently than MYLS22. These chemical probes validate OPA1 as a therapeutic target to increase cancer cell apoptosis at the mitochondrial level.

INTRODUCTION

Mitochondria are crucial organelles in intermediate metabolism, energy conversion, signaling, and apoptosis. Our understanding of their role in cell biology has been paralleled by an extension of the concept of mitochondrial participation in cancer. Originally, mitochondrial role in cancer was restricted to their function as platforms for the execution of apoptosis (*1*), the dysregulation of which is a hallmark of cancer (*2*). Now, mitochondria are increasingly recognized as essential signaling units in the key neoplastic processes of differentiation (*3*), autophagy (*4*), epigenetic stability and epithelial-mesenchymal transition (*5*), and migration (*6*). Mitochondrial dynamics, i.e., the mitochondrial membrane shape changes controlled by mitochondria-shaping large dynamin-related guanosine triphosphatases (GTPases), is involved in most of these processes (*7*). Originally, mitochondrial dynamics was also linked to cancer because of its role in apoptosis. The Bcl-2–controlled process of mitochondrial cytochrome c release to activate caspase-9 and other downstream caspases that execute the orderly demise of the cell is accompanied by mitochondrial fragmentation and requires cristae remodeling (*7*), a mitochondrial ultrastructural reorganization that allows complete cytochrome c release, essential in cancer cells for caspase activation (*8*). Both processes are controlled by mitochondria-shaping proteins that impinge on organelle fusion and fission processes. Mitochondrial division is regulated by dynamin-related protein (Drp) 1, mitochondrial fission factor (Mff), and fission (Fis) 1. Mitofusins (Mfn) 1 and 2 in the outer membrane and Optic Atrophy 1 (Opa1) in the inner membrane control mitochondrial fusion. Opa1 levels and GTPase function are required, or mitochondrial fusion (*9*) and independently from mitochondrial fusion, for cristae biogenesis (*10*) to inhibit cristae remodeling and hence cytochrome c release and apoptosis (*11*–*14*), to control mitochondrial respiration and cell growth (*15*), and to modulate differentiation (*3*).

OPA1 is overexpressed in several types of cancer. *OPA1* is located on chromosome 3q28, a region comprised in the 3q26-3q28 amplicon, a hallmark of lung cancer (*16*). *OPA1* copy number alterations are retrieved in ~30% of sequenced aerodigestive trait (e.g., lung and esophagus) cancer specimens that are frequently characterized by the 3q26-3q28 amplicon (*16*, *17*). *OPA1* was identified as one of the eight prognosis-related genes that exhibit high alteration frequency and amplification across pan-cancer, including breast cancer where *OPA1* was also notably overexpressed (*18*). Increased Opa1 levels negatively correlate with sensitivity to classic chemotherapy and survival rates (*19*–*21*), nominating Opa1 as a target to overcome chemoresistance and cancer cell response to targeted therapeutics is accordingly augmented by *OPA1* deletion (*17*). For example, *OPA1* is up-regulated in in acute myeloid leukemias (AMLs) resistant to the Bcl-2 antagonist venetoclax and *OPA1* deletion normalizes venetoclax sensitivity (*22*). Last, endothelial *Opa1* is required for cancer angiogenesis and its deletion curtails tumor growth and metastatization (*23*). Because Opa1 function depends on its GTPase activity, we explored the possibility that chemical inhibition of Opa1 GTPase activity could mimic *OPA1* deletion and reported that heterocyclic *N*-pyrazole derivative MYLS22 faithfully reproduced the effects of *Opa1* deletion in endothelial cells or in xenografted human metastatic breast cancer cells to blunt tumor growth (*23*, *24*). Since then, MYLS22 has been used successfully to revert chemoresistance in breast cancer (*25*) and lung adenocarcinoma (*26*) and to reduce the burden of AML in vitro and from patient-derived xenografts, without affecting normal hematopoietic cells (*27*). However, despite

[1]Veneto Institute of Molecular Medicine, Via Orus 2, 35129 Padova, Italy. [2]Department of Biology, University of Padova, Via U. Bassi 58B, 35121 Padova, Italy. [3]Department of Pharmaceutical and Pharmacological Sciences, University of Padova, Padova, Italy. [4]Molecular Modeling Section, Department of Pharmaceutical and Pharmacological Sciences, University of Padova, Padova, Italy. [5]Departments of Biochemistry and Medicine, Albert Einstein College of Medicine, Bronx, NY, USA.
*Corresponding author. Email: luca.scorrano@unipd.it
†Present address: Friede Springer Cardiovascular Prevention Center at Charité, Hindenburgdamm 30 Haus IIIA, 12203 Berlin, Germany.
‡Present address: Astria Therapeutics, 22 Wharf Rd., Boston, MA 02210, USA.
§Present address: GIGA-Cancer, Laboratory of Mitochondria and Cell Communication, University of Liege, Av. Hippocrate 1/11, B-4000 Liège, Belgium.

its wide use, MYLS22 is poorly characterized. Its specificity for its putative target Opa1 is unclear. This molecule is poised by low water solubility and, as such, displays variable efficacy that apparently depends on the experimental settings. It is also unknown if it can be used as a scaffold to evolve more powerful and soluble Opa1 inhibitors. By an in vitro high-throughput screening (HTS) assay on recombinant, purified Opa1 (rOpa1) (*28*) GTPase activity, we identify the prototypical Opa1 inhibitor MYLS22 and evolve it by structure-activity relationship (SAR) analysis into more potent and specific Opa1 inhibitors (Opitors). MYLS22 and Opitors highlight the role of Opa1 in cytochrome c release and resistance to Bcl-2 inhibitors in triple-negative breast cancer (TNBC).

RESULTS

An HTS identifies inhibitors of rOPA1 GTPase activity

We conducted an in vitro HTS to identify small molecules that inhibit the GTPase activity of a purified recombinant Opa1 protein (rOpa1). This rOpa1 corresponds to the *Mus musculus* isoform 1 (UniProt: P58281), lacking the mitochondrial targeting sequence and the transmembrane domain (amino acids 1 to 167), and fused to a C-terminal 6X His-tag (*28*). By reversed-phase chromatography (RPC), we measured rOpa1 kinetics parameters ($K_m = 170.4 \pm 46.4$ μM/min, $V_{max} = 0.5 \pm 0.03$), which were consistent with other dynamin-like proteins in the absence of vesicles (*29*) and exhibited minimal batch variability (fig. S1A). To measure the enzymatic activity of rOpa1 in an HTS, we used the malachite green (MG) colorimetric assay, which quantifies the free phosphate released during the hydrolysis of guanosine triphosphate (GTP) into guanosine diphosphate (GDP) (*30*). Kinetic properties of rOpa1 measured with the MG assay were superimposable to those obtained by RPC, were sensitive to the concentration of Mg^{2+} in the assay buffer, unaffected by dimethyl sulfoxide (DMSO), and inhibited by nonhydrolyzable GTP analog GTP-γ-S [guanosine 5′-*O*-(3′-thiotriphosphate)] as well as by the Mg^{2+} chelating agent EDTA that can therefore serve as a negative control when using the MG assay to screen for Opa1 inhibitors (fig. S1, A to D). We adjusted the MG assay for HTS by optimizing the enzyme-to-substrate ratio (rOpa1/GTP) to enhance sensitivity without compromising detection specificity, and we designed a semiautomated 384-well plates HTS pipeline of a library of 10,191 drug-like small molecules (MyriaScreen Diversity Library II, Aldrich), selected based on their compliance with Lipinski's "Rule of Five" (Fig. 1A and table S1). The compounds (at a final concentration of 50 μg/ml) were incubated for 1 hour with rOpa1, and the amount of free phosphate released during the hydrolysis of GTP was determined using the colorimetric MG assay. We applied graphical and statistical quality controls to validate our HTS pipeline, ensuring that positive hits could be distinguished from assay noise. By using the strictly standardized mean difference (SSMD) to assess the strength of differences between positive (i.e., maximal rOpa1 inhibition) and negative (i.e., minimal Opa1 inhibition) control samples, only plates with SSMD ≤ -3 can pass quality control (*31*). In our screening, the assay was sufficiently robust, with only four plates failing quality control (fig. S1E). Plotting raw data from the 32 assayed 384-well plates against the well numbers, we observed a robust assay window between positive (EDTA) and negative (2.5% DMSO) controls, even if negative controls spanned a larger range of values than the positive controls. The scatterplot indicated two distinct populations: a majority of compounds that did not inhibit rOpa1 and a second population of active molecules inhibiting rOpa1 at levels falling between negative and positive controls (fig. S1F). Raw data were normalized to percent activity (NPA) relative to negative controls, and a trellis heatmap was created, showing wells color coded from dark red (high inhibition) to dark blue (low inhibition). The heatmap revealed no systematic patterns suggestive of compound delivery errors (fig. S1G).

We performed two rounds of screening and calculated the normalized percent inhibition (NPI) for each well (k_i) relative to positive controls for each replicate (NPI_{ki}). The NPI_{ki} values were then standardized with Z_{ki} scores, considering the median and the median absolute deviation (MAD) of sample values across all plates of one replicate experiment. By ranking the tested compounds for their Z_{ki} values, we found that most fell in the NPI range of the negative controls. Compounds with an average $Z_{ki} < 0.7$, i.e., decreasing Opa1 activity by at least 30% in both replicates (red dots in Fig. 1, B and C), were designated as inhibitors. By excluding false positives and PAINS (Pan-Assay Interference) and retaining only the compounds identified in both repeats, we identified eight potential rOpa1 GTPase activity inhibitors (Fig. 1D and table S2).

We tested the eight selected compounds purchased from a different vendor in dose-response experiments (from 1 nM to 750 μM) to confirm their effect and select the most potent molecule. Four compounds truly inhibited rOpa1 GTPase activity in a concentration-dependent manner, with Hill coefficient > 1, indicating positively cooperative binding. Among these four molecules, the heterocyclic *N*-pyrazole derivative *N*-(1,5-dimethyl-3-oxo-2-phenyl-2,3-dihydro-1*H*-pyrazol-4-yl)-3-methyl-1-PH+ (MYLS22) was the most potent inhibitor [median inhibitory concentration (IC_{50}) = 82.4 ± 6.2 μM; $I_{max} = 0.9$] (Fig. 1F). In conclusion, we identified in vitro inhibitors of rOpa1 GTPase activity, MYLS22 being the most potent hit.

MYLS22 is a cell-permeable lipophilic small molecule that does not cause cell death or mitochondrial toxicity

Discrepancies between the results obtained in biochemical and cell-based assays have traditionally been attributed to low permeation of identified hits across the cellular membrane (*32*). MYLS22 is a drug-like molecule that meets all the physicochemical requirements of Lipinski's Rule of Five (*33*). Although it is characterized by low aqueous solubility (calculated log $P = 3.51$), MYLS22 was readily soluble in DMSO up to 20 mM and in Dulbecco's modified Eagle's medium (DMEM) cell culture medium up to 150 μM. Because MYLS22 is not fluorescent, we could not directly visualize its cellular uptake and distribution. Nevertheless, we succeeded in measuring the accumulation of MYLS22 in cells using two independent and complementary methods by exploiting its absorbance at 280 nm.

First, we incubated mouse embryonic fibroblasts (MEFs) with MYLS22 in Hanks' balanced salt solution (HBSS) and measured the remaining amount of MYLS22 in the extracellular medium (using its 280-nm absorption as a proxy) over time. The concentration of MYLS22 decreased with incubation time (fig. S2A). Because this decrease could be due to nonspecific binding to the culture dish, to verify that MYLS22 entered cells, we used ultraviolet reversed-phase high-performance liquid chromatography (HPLC) on cell lysates preprocessed with solid-phase extraction (SPE) optimized to ensure that the retention time of the inhibitor did not overlap with any other components of the cell lysates. We successfully isolated the elution peak of MYLS22, detected by its absorbance at 280 nm, in a total run time of 15 min. At an input concentration of 100 μM, we

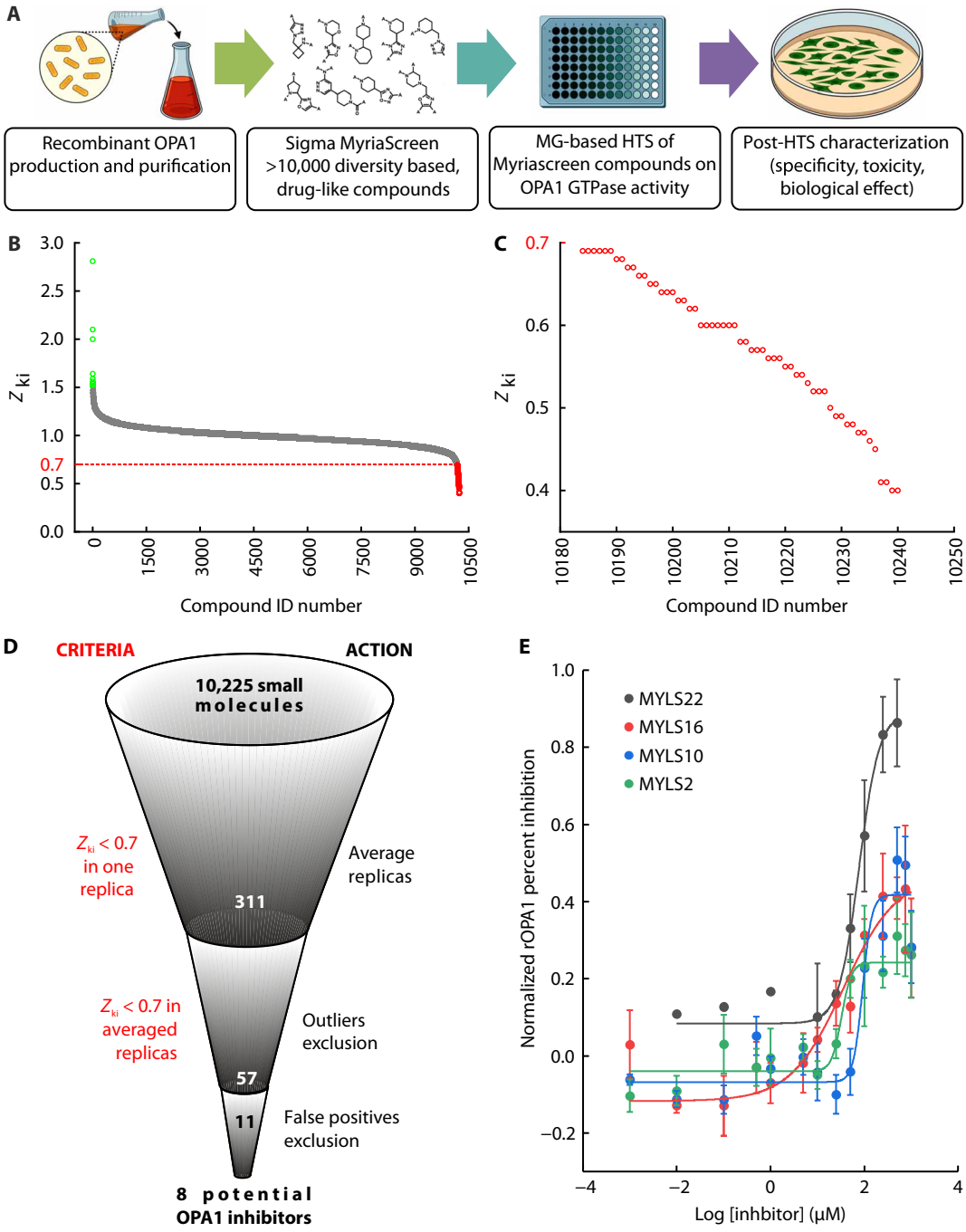

Fig. 1. An HTS identifies potential Opa1 GTPase inhibitors. (**A**) Schematic workflow of the key steps for identifying small-molecule inhibitors of Opa1 GTPase activity. The process includes (i) production, purification, and characterization of recombinant Opa1 protein (rOpa1); (ii) selection and preparation of a diverse-based library of drug-like small molecules; (iii) HTS to evaluate the effect of each compound on rOpa1 activity using the colorimetric MG GTPase assay; and (iv) data analysis, hits identification, and characterization (assessment of the mechanism of action, biological effects, potency, specificity, and SAR analysis). (**B**) Z_{ki} values for each compound against its ID number. The dashed line at $Z_{ki} = 0.7$ denotes the threshold for identifying compounds with at least 30% inhibition of Opa1 GTPase activity. Data represent the average of two HTS replicates. (**C**) Magnified view of (B), focusing on compounds with Z_{ki} values < 0.7 (red circles) that were selected for further analysis. (**D**) Flowchart illustrating the selection process for Opa1 inhibitors. Of the 10,225 initial compounds, 8 were identified as potential Opa1 inhibitors and advanced to subsequent analysis. (**E**) Dose-response curves of the NPI of rOpa1 GTPase activity by the four selected potential OPA1 inhibitors. Data are normalized using EDTA as a positive control and DMSO (vehicle) as a negative control. Values represent means ± SEM of four independent biological replicates ($n = 2$ technical replicates per biological replicate). Nonlinear dose-response curves were fitted using the Levenberg-Marquardt iteration algorithm to the data to determine the IC_{50}, maximum inhibition (I_{50}), and the parameters to calculate the Hill coefficient.

detected ~20 μM MYLS22 in the cellular lysate (fig. S2B). Although it is plausible to conclude that only 20% of the administered MYLS22 is internalized after 24 hours, direct HPLC measurements are limited in that they do not account for potential and likely cellular MYLS22 catabolism. After 14 hours, 71.4% of added MYLS22 was not measured in the extracellular medium (fig. S2A). We next assessed MYLS22 cytotoxicity and found that concentrations up to 100 μM did not significantly reduce MEF viability (fig. S2C). Because cultured cells can survive mitochondrial dysfunction by operating the reversal mode of the adenosine triphosphate (ATP) synthase (*28*), we measured mitochondrial membrane potential in response to the F_1F_o adenosine triphosphatase (ATPase) inhibitor oligomycin, a sensitive test of latent mitochondrial dysfunction in cells (*34*). Real-time imaging of the mitochondrial potentiometric dye tetramethyl rhodamine methyl ester (TMRM) fluorescence in response to oligomycin treatment showed a stable membrane potential in MEFs treated with MYLS22 over a range of concentrations well above rOpa1 IC_{50} (fig. S2D). We further confirmed the lack of mitochondrial toxicity in vitro by using mitochondria purified from mouse liver. Regardless of whether mitochondria were energized using substrates feeding complex I (glutamate/malate; fig. S2E) or complex II (succinate; fig. S2F), MYLS22 did not reduce the uptake of the potentiometric dye Rhodamine 123 and hence membrane potential. We lastly addressed whether reactive oxygen species (ROS) accumulated in cells treated with MYLS22 using the fluorescent dye MitoSOX. Whereas antimycin A (AA), which stimulates ROS production by interfering with the Q cycle in complex III resulted in the expected MitoSOX fluorescence increase, MYLS22 did not (fig. S2G). In conclusion, we defined a safe range of MYLS22 concentrations for assessing inhibitor-specific cellular functions without cytotoxic and mitochondriotoxic effects.

MYLS22 induces mitochondrial fragmentation and cristae remodeling

Next, we addressed the biological effects of MYLS22 on the key parameters controlled by Opa1 GTPase activity, essential for mitochondrial fusion and ultrastructure. Mitochondria in *Opa1*$^{-/-}$ cells or expressing dominant-negative GTPase Opa1 mutants are fragmented and their cristae sparse and remodeled (*9*, *11*, *35*–*38*). These phenotypes should be reproduced upon Opa1 inhibition by a small molecule. After 5 hours of incubation, MYLS22 caused a dose-dependent mitochondrial fragmentation in MEFs expressing mitochondrially targeted yellow fluorescent protein (mtYFP), phenocopying the dot-like mitochondria observed in *Opa1*$^{-/-}$ MEFs (Fig. 2, A and B). As judged by electron microscopy (EM), treatment with MYLS22 did not cause nuclear pyknosis, plasma membrane permeabilization, or dilatation of the endoplasmic reticulum (ER), an early proxy of ER stress (Fig. 2C). Conversely, mitochondria appeared shorter and their cristae structure disrupted. Morphometric analysis showed that, in MYLS22-treated cells, mitochondrial cristae were less, and in the remaining cristae, the lumen was enlarged and the number of cristae junction was reduced (Fig. 2, D to G). These findings confirm that MYLS22 is not per se cytotoxic, yet it replicates the effects of Opa1 deletion on mitochondrial morphology and ultrastructure.

MYLS22 is a specific OPA1 GTPase inhibitor in vitro and in cells

A major limitation of GTPase inhibitors is their off-target activity due to the high degree of conservation of the GTPase domain as observed in the dynamin superfamily proteins (fig. S3A). We therefore used a multipronged approach to verify MYLS22 specificity. First, because the catalytic GTP pocket of Opa1 is highly conserved within the dynamin superfamily proteins (fig. S3A), we measured the inhibitory activity of MYLS22 on Dynamin-1 (Dyn1), one of the closest OPA1 homologs. Unlike MYLS2, a different potential OPA1 inhibitor found in the HTS that inhibited a recombinant Dynamin-1 protein lacking the proline-rich domain (PRD) (Dyn1ΔPRD), MYLS22 did not affect Dyn1ΔPRD activity even at concentrations 10 times higher than the IC_{50} for OPA1 (Fig. 3A).

We next assessed whether MYLS22 directly interacted with the G domain of Opa1 in solution to inhibit its catalytic activity. We produced a minimal version of the rOpa1 used for the in vitro screening (mini-rOpa1), composed of the Opa1 GTPase domain linked to the Bundle Signaling Element (BSE) domain of its GTPase effector domain (GED) (fig. S3, B and C). We performed saturation transfer difference (STD) nuclear magnetic resonance (NMR) experiments. The off-resonance spectrum of the aromatic region of MYLS22 in the presence of the mini-rOpa1 domain exhibited narrow and well-resolved lines. By subtracting the on-resonance spectrum from the off-resonance reference spectrum, we obtained the STD difference spectrum, revealing specific, albeit modest, signals confirming the MYLS22–mini-rOpa1 G domain interaction (Fig. 3B). Unfortunately, MYLS22 was not soluble enough to produce clear spectrum peaks for the identification of the binding epitope. To elucidate the potential binding mode of MYLS22 to Opa1, we performed a molecular docking study. MYLS22 was docked into the GDP-binding site of Opa1 [Protein Data Bank (PDB): 6JTG], and the predicted poses were ranked and rescored using the Molecular Mechanics-Generalized Born Surface Area (MM-GBWSA) method following optimization of both the ligand and binding pocket. The best-scoring pose of MYLS22 was located within the GTP-binding pocket, largely overlapping with the GDP site (Fig. 3C and movie S1). Specifically, the phenyl-thienopyrazole moiety occupied a key region involved in guanine base recognition, whereas the antipyrine moiety resided in the phosphate recognition subsite, bordered by the G1/P-loop and G2/switch1. The docking model further suggested potential hydrogen bonds with Ser^{298}, Gly^{300}, and Lys^{301}, along with arene-hydrogen interactions involving Lys^{468}, Lys^{301}, and Met^{322} (Fig. 3D). To validate these predictions, we generated mini-rOpa1 mutants of the residues predicted to interact with MYLS22, thereby disrupting the ligand-protein interface, and assessed their impact on binding and inhibitory activity. However, because these residues are essential for GTP/GDP binding and hydrolysis, the mutants were catalytically inactive. In addition, we mutated two residues in the β6-α5 loop surrounding the binding site, producing mini-rOpa1^{T503A} and mini-rOpa1^{K505N}. Whereas the GTPase activity of mini-rOpa1^{T503A} was significantly impaired, that of mini-rOpa1^{K505N} remained unaffected (Fig. 3E). Notably, MYLS22 inhibited mini-rOpa1 GTPase activity similarly to rOpa1, indicating that MYLS22 effects are retained even in the absence of all OPA1 domains except for the GTPase and GED present in mini-rOpa1. However, MYLS22 failed to inhibit the in vitro GTPase activity of mini-rOpa1^{K505N} (Fig. 3F), indicating that an intact K505 residue is critical for MYLS22-mediated inhibition.

We next evaluated whether MYLS22 could interact with Opa1 in intact cells by cellular thermal shift assay (CETSA) (*39*–*41*), a biophysical technique that exploits ligand-induced thermal stabilization of proteins upon direct target engagement in cells. Five hours after MEF treatment with MYLS22, we observed a rightward shift of the thermal melting curve of Opa1, with a significant protein stabilization

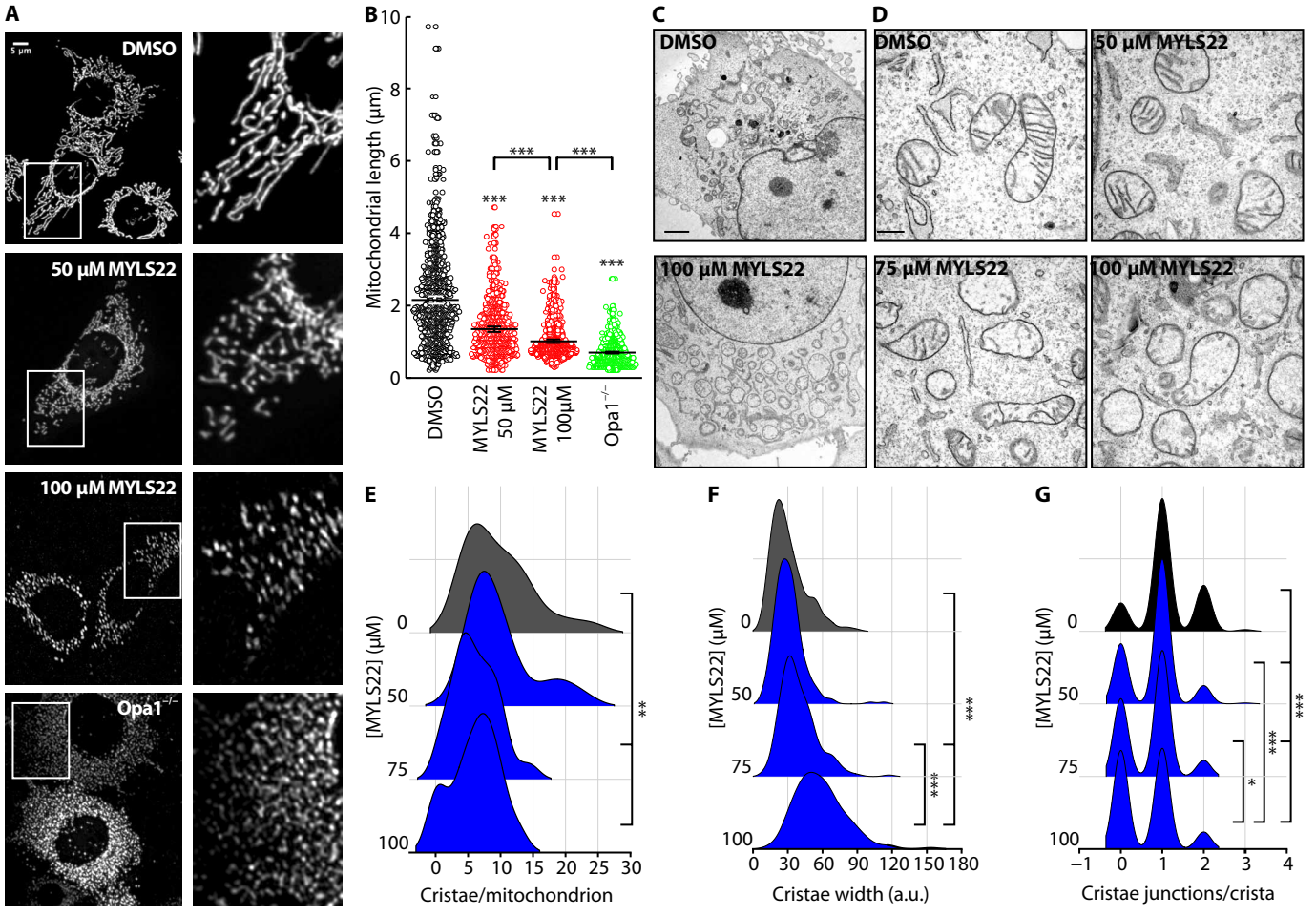

Fig. 2. MYLS22 induces mitochondrial network fragmentation and cristae disruption. (**A**) Representative confocal images of WT or Opa1$^{-/-}$ MEFs expressing mtYFP treated as indicated for 12 hours. Scale bar, 5 µm. The boxed area is magnified 2.8X on the right. (**B**) Quantification of the mitochondrial major axis length in experiments as in (A). Data are presented as a dot plot, with each dot representing an individual mitochondrion (n = 700 to 900 mitochondria per condition). Means ± SEM from four biological replicates is overlaid. ***P < 0.001 in a one-way Kruskal-Wallis ANOVA between the indicated conditions or when not indicated with DMSO. (**C** and **D**) Representative EM micrographs of WT MEFs treated for 12 hours as indicated. Scale bars, 1 µm in (C) and 500 nm in (D). (**E**) Ridgeline chart of the cristae number per mitochondrion in experiments as in (D). N = 25 to 50 mitochondria per condition from three biological replicates. **P < 0.01 in a one-way Kruskal-Wallis ANOVA between the indicated conditions. (**F**) Ridgeline chart of the mitochondrial cristae width in experiments as in (D). N = 225 cristae per condition from three biological replicates. ***P < 0.001 in a one-way Kruskal-Wallis ANOVA between the indicated conditions. a.u., arbitrary units. (**G**) Ridgeline chart of the cristae junction number per crista in experiments as in (D). N = 200 to 300 cristae per condition from three biological replicates. *P < 0.05 and ***P < 0.001 in a one-way Kruskal-Wallis ANOVA between the indicated conditions.

at higher temperatures compared to when we treated cells with DMSO. In contrast, the thermal denaturation curve of actin remained unaltered in the presence of MYLS22 (Fig. 4, A and B). Overall, MYLS22 treatment increased the temperature at which 50% of the initial Opa1 amount is recovered in the soluble fraction by nearly 4°C, thereby indicating its target engagement in situ. Moreover, MYLS22 did not affect levels or activation of other components of the fusion/fission machinery (Fig. 4C). Next, we reconstituted *Opa1*$^{-/-}$ MEFs with a bicistronic vector expressing wild-type (WT) or K505N Opa1 together with mtYFP. Whereas MYLS22 caused the expected mitochondrial fragmentation in MEFs reconstituted with Opa1^{WT}, the mitochondrial network was unaffected in cells expressing the Opa1^{K505N} mutant unable to bind MYLS22 (Fig. 4, D and E). Together, these results indicate that MYLS22 is a specific inhibitor of Opa1 GTPase activity that causes mitochondrial fragmentation by engaging with its target in vitro and in cells.

SAR-driven evolution of MYLS22

To validate and enhance the inhibitory activity of MYLS22 (IC_{50} = 82.4 ± 6.2 µM), we performed an in silico screening of 300 diverse small molecules docked onto the mini-Opa1 structure. These compounds belonged to two different series of analogs generated by modifying each of the two MYLS22 core regions: the thieno-pyrazole and the antipyrine scaffold (Fig. 5A). Our computational screening yielded 16 candidate compounds, designated as Opa1 inhibitors (Opitors) 0 to 15 (table S3), which we subsequently synthesized and tested for mini-rOpa1 GTPase activity inhibition.

These SAR studies indicate that three factors are critical for achieving potent Opa1 inhibition: (i) the presence of the phenyl group on the thieno-pyrazole scaffold, (ii) a negative charge at the position of the molecule that interacts with Opa1 GTPase pocket, and (iii) specific modifications to the antipyrine moiety. Modifications to the phenyl substituent on the thieno-pyrazole (Opitor-10 to Opitor-15)

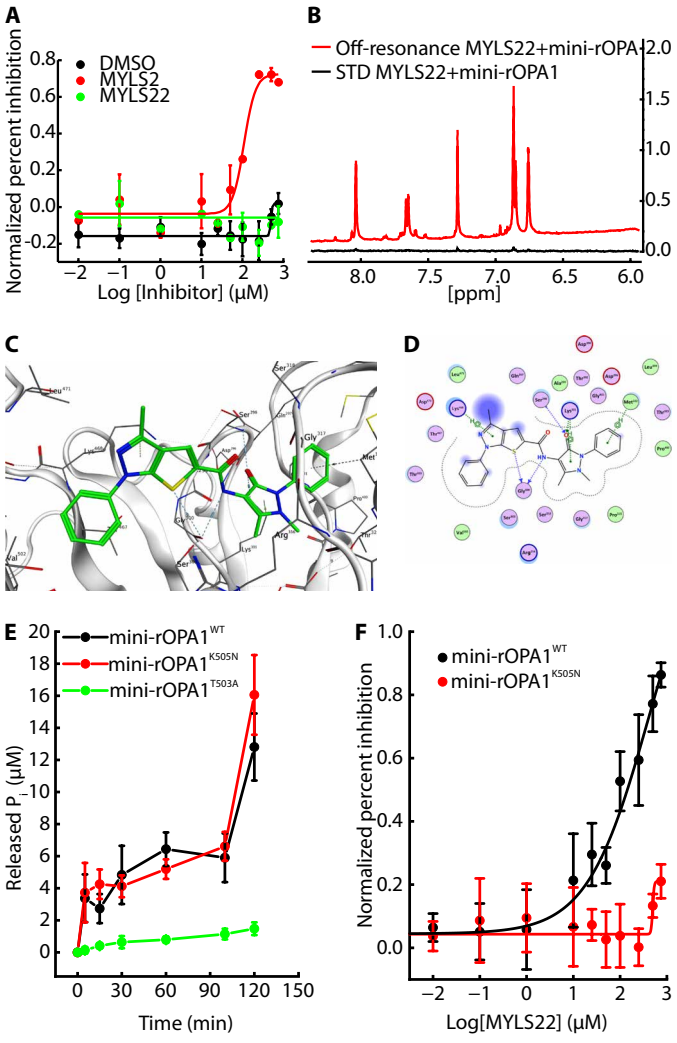

Fig. 3. Inhibition of recombinant OPA1 by MYLS22 is contingent upon the intactness of its binding site. (**A**) Dose-response curves of recombinant Dynamin-1 (0.5 μM Dyn1ΔPRD) GTPase activity after incubation with the indicated concentrations of the indicated compounds. Values represent means ± SEM of three independent biological replicates ($n = 2$ technical replicates per biological replicate). Nonlinear dose-response curves were fitted using the Levenberg-Marquardt iteration algorithm to the data. (**B**) Representative traces of biophysical detection of mini-rOpa1-MYLS22 interaction by ^{1}H-NMR STD. The ^{1}H-NMR STD transfer experiment shows the aromatic protons of 100 μM MYLS22 in the presence of 2 μM mini-rOpa1 (red spectrum), whereas the black spectrum represents the STD NMR difference spectrum of MYLS22 after selective saturation of mini-rOpa1 ^{1}H methyl resonances. (**C**) Best-scoring binding pose of MYLS22 (green) in the GTPase pocket of Opa1 (PDB ID: 6JTG; white ribbon) obtained from molecular docking calculations. (**D**) 2D depiction of the interaction between MYLS22 and Opa1 in the pose shown in (C). Key noncovalent interactions stabilizing the binding are highlighted. Color-coded spheres represent the different amino acid types: polar (purple), acid (purple-red), basic (purple-blue), and hydrophobic (green). Interactions are indicated as color-coded lines: hydrogen-arene (dotted green) and hydrogen bonds (dotted blue). Ligand exposure to solvent is reported as a blue shadow. (**E**) Kinetics of GTP hydrolysis by the indicated recombinant mini-rOpa1 mutants (1 μg) measured by MG assay. Data represent means ± SEM of $n = 3$ biological replicates. (**F**) NPI of the GTPase activity of the indicated mini-rOpa1 mutants by MYLS22. Values represent means ± SEM of three biological replicates ($n = 2$ technical replicates per biological replicate). Nonlinear dose-response curves were fitted in OriginPro using the Levenberg-Marquardt iteration algorithm to the data.

or removal of the antipyrine moiety (Opitor-5) completely abolished activity, highlighting the essential role of the thieno-pyrazole phenyl group and the presence of the antipyrine scaffold. Conversely, substituting the antipyrine *N*-methyl with a benzyl group in Opitor-0 enhanced inhibition ($IC_{50} = 3.0 \pm 1.6$ μM). The replacement of the antipyrine scaffold with alternative cores yielded eight compounds (Opitor-1 to Opitor-9). Poor water solubility led to the exclusion of Opitor-4, Opitor-6, and Opitor-8 from further studies. Molecular docking suggested that an *N*-piperidinyl amide, particularly when substituted at position 4, was a promising replacement for antipyrine. We found that only piperidine and piperazine derivatives (Opitor-1, Opitor-2, Opitor-3, Opitor-4, and Opitor-7) featuring a carboxylate at position 4 exhibited potent activity. Opitor-3, with an IC_{50} of 1.5 ± 1.3 μM (despite a reduced I_{max} of 0.7 ± 0.0), demonstrated that the carboxylate can act as a bioisostere of the phosphate in the GTPase site. Compounds lacking this negative charge (Opitor-2, the ethyl ester derivative of Opitor-3, Opitor-1, and Opitor-7) were inactive, confirming that a negative charge is essential for effective Opa1 inhibition. Last, the introduction of a tetrazole scaffold yielded Opitor-9 and its *N*1-methyl derivative Opitor-8. Opitor-9 exhibited enhanced activity ($IC_{50} = 1.3 \pm 1.1$ μM) but with a lower I_{max} (0.7 ± 0.1). In contrast, the *N*1-methylated derivative, with an increased pK_a (where K_a is the acid dissociation constant) that disfavors a negative charge, showed diminished activity, further reinforcing the importance of the negative charge in the phosphate binding site (fig. S4 and table S3). We confirmed that Opitor-0, which exhibits the highest I_{max}, and Opitor-3, which combines excellent solubility with high potency, inhibited mini-rOpa1 GTPase activity at concentrations 2 log lower than MYLS22 (Fig. 5B). Moreover, Opitor-0 that docked on Opa1 in a best-scoring pose very similar to that of MYLS22 (fig. S5, A and B, and movie S2) was also unable to inhibit the mini-rOpa1^{K505N} mutant in the MYLS22 binding site (Fig. 5B).

Because Opitor-3 exhibited remarkable water solubility, we proceeded with its biophysical characterization using NMR to confirm binding and assess the binding epitope. We first conducted WaterLOGSY experiments. In the presence of mini-rOpa1, the signals of Opitor-3 phase matched with those of mini-rOpa1 (both negative), whereas in its absence, the signals inverted phase. This inversion indicated that Opitor-3 acquires protein magnetization through intermolecular nuclear Overhauser effects (NOEs), a clear signature of protein-ligand complex formation (fig. S5A). Given the well-dispersed signals of Opitor-3, we also performed STD NMR experiments to pinpoint the ligand binding epitope. Our molecular docking predicted that that the methyl group and the unique aromatic hydrogen were the most solvent exposed in the proposed binding pose (fig. S5, B and C). In the STD NMR analysis, these epitopes displayed the lowest STD effects, suggesting that these protons are minimally involved in the interaction with mini-rOpa1 (fig. S5D). These results establish that Opitor-3 binds to mini-rOpa1 via a well-defined epitope that excludes the methyl group and the unique aromatic hydrogen of the thieno[2,3-*c*]pyrazole core (fig. S5E).

We further characterized Opitor-0 and Opitor-3 in cells. Confocal imaging of mtYFP-expressing MEF cells showed that both compounds induced mitochondrial fragmentation in a concentration-dependent manner, with activity observed even in the nanomolar range (fig. S6, A and B). However, in human HeLa cells, the efficacy of Opitor-3 was markedly reduced, whereas Opitor-0 continued to outperform MYLS22 (Fig. 5, D and E, and lower magnification images in fig. S6C).

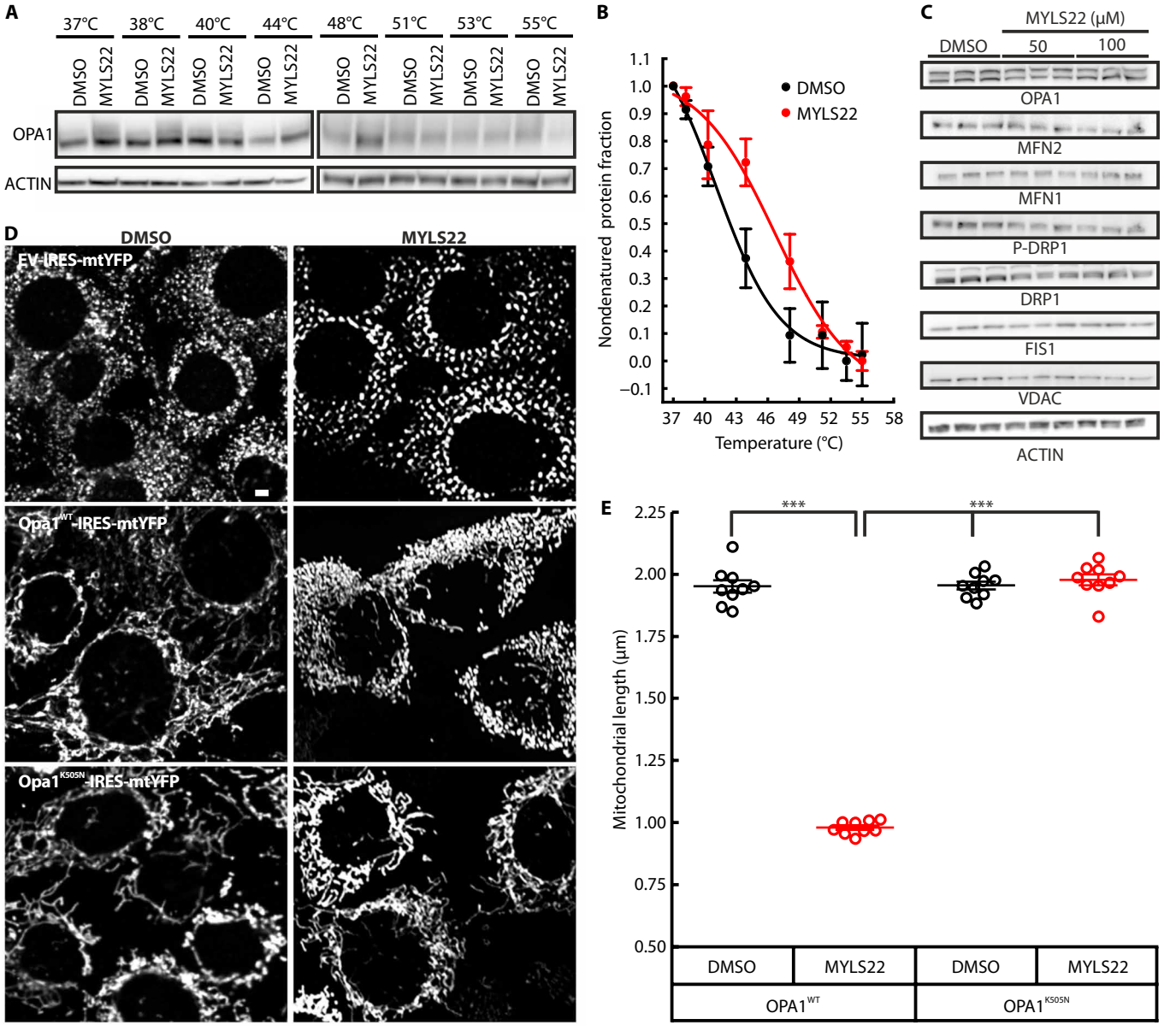

Fig. 4. MYLS22-induced mitochondrial fragmentation requires intactness of its Opa1 binding site. (**A**) MEFs were treated for 5 hours with 100 μM DMSO or MYLS22, and equal amounts of lysates were heated for 3 min at the indicated temperatures. Lysates were then separated by SDS-PAGE and immunoblotted using the indicated antibodies. (**B**) Average ± SEM of nondenatured Opa1 fraction in four independent CETSA experiments as in (A). Nonlinear dose-response curves were fitted in OriginPro using the Levenberg-Marquardt iteration algorithm to the data. (**C**) MEFs treated for 5 hours as indicated were lysed, and equal amounts of lysates were separated by SDS-PAGE and immunoblotted using the indicated antibodies. Each lane represents a biological replicate. (**D**) Representative confocal images of mtYFP in *Opa1*$^{-/-}$ MEFs transfected with the indicated plasmids. Original images were digitally enlarged 2.8X to enhance mitochondrial visualization. Where indicated, cells were treated with 100 μM MYLS22 for 6 hours. Scale bar, 10 μm. (**E**) Means ± SEM of the major axis length of mitochondria in $n = 10$ biological replicates (dots) of experiments as in (C) ($n \approx 100$ mitochondria per condition). ***$P < 0.001$ in a one-way Kruskal-Wallis ANOVA between the indicated conditions.

Thus, our SAR studies identified Opitor-0 as a more potent MYLS22 analog that effectively induces mitochondrial fragmentation in both human and mouse cells, representing a valuable probe to explore the role of Opa1 in chemoresistance.

MYLS22 and Opitor-0 enhance mitochondrial cytochrome c release

Evasion from apoptosis is a hallmark of cancer cells and represents a key feature of resistance to conventional and targeted therapies. Independently of its role in mitochondrial fusion, Opa1 inhibits maximal cytochrome c release, a process that requires the integrity of its GTPase domain (*11*), with high levels of Opa1 conferring resistance to apoptosis (*11*, *42*–*44*). We therefore investigated whether MYLS22 and Opitor-0 could enhance cytochrome c release. The amount of cytochrome c released from purified mouse liver mitochondria in response to the active form of the proapoptotic Bcl-2 molecule BID (cBID) (*11*) was increased when mitochondria were coincubated with MYLS22, as measured by immunoblotting (Fig. 6A)

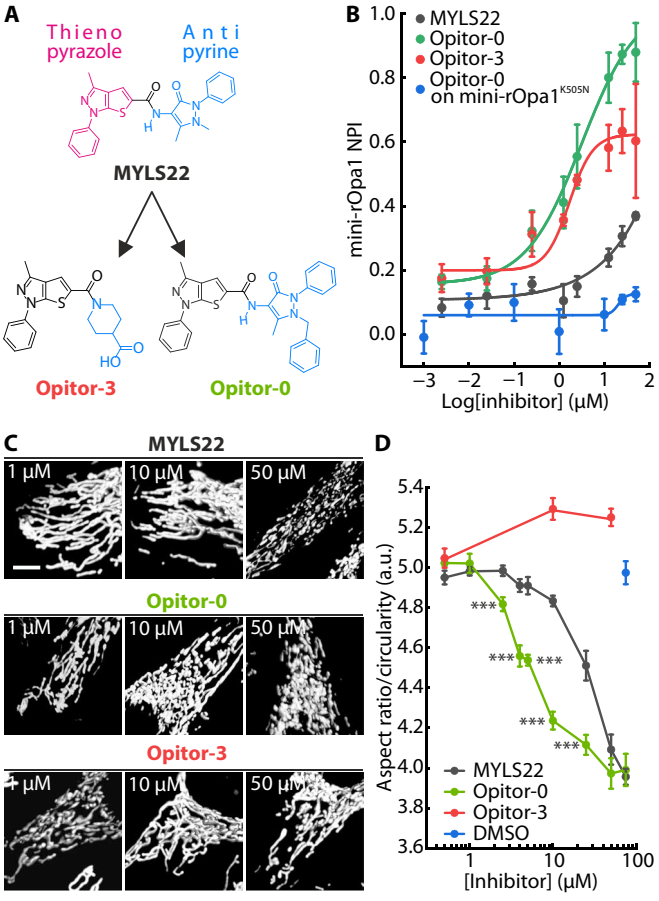

Fig. 5. SAR-driven evolution of MYLS22 to Opitor-0, a more potent Opa1 inhibitor. (**A**) Chemical structures of MYLS22 and its derivatives Opitor-0 and Opitor-3. The thieno-pyrazole (purple) and the antipyrine (blue) groups are indicated. (**B**) NPI of the GTPase activity of WT and the indicated mini-rOpa1 mutant by the indicated compounds. Values represent means ± SEM of four independent biological replicates (n = 2 technical replicates per biological replicate). Nonlinear dose-response curves were fitted to the data in OriginPro to determine the IC_{50}. (**C**) Representative 3X magnified regions of volume rendered reconstructions of z-stacks of confocal images of mtYFP in HeLa::mtYFP cells treated as indicated for 5 hours. The images corresponding to the full reconstruction of the indicated cells and the DMSO-treated control are shown in fig. S6. Scale bars, 5 μm. (**D**) Quantification of mitochondrial length in n = 5 biological replicates of experiments as in (D) (~100 mitochondria analyzed per condition). Data represent means ± SEM. ***P < 0.001 in one-way Kruskal-Wallis ANOVA comparing each concentration of MYLS22 with Opitor-0.

and a quantitative cytochrome c enzyme-linked immunosorbent assay (ELISA) (Fig. 6B). MYLS22 enhanced the cBID-mediated disruption of chemically cross-linkable OPA1 oligomers, destabilized during cristae remodeling and complete cytochrome c release (*11*) (Fig. 6C). We then examined whether MYLS22 also enhanced cytochrome c release in a cell-based assay. MYLS22-treated MEFs exhibited more rapid cytochrome c release in response to the intrinsic apoptotic stimulus H_2O_2 (*45*), achieving maximal release within 30 min after apoptosis induction (Fig. 6, D and E). We then compared Opitor-0 with MYLS22. Opitor-0 outperformed MYLS22 in enhancing cytochrome c release in response to cBID, increasing it already at 10 μM (Fig. 6F). In conclusion, MYLS22 facilitates mitochondrial cytochrome c release in response to apoptotic stimuli and its analog Opitor-0 shows superior potency and efficacy.

MYLS22 and Opitor-0 revert breast cancer cell resistance to Bcl-2 inhibition

Chemoresistance is a common side effect of conventional and targeted cancer therapies. A considerable proportion of TNBCs develop resistance to taxanes after an initial response (*46*). Inhibitors of the key anti-apoptotic molecule Bcl-2, such as ABT-737 and venetoclax (*47*, *48*), can reverse paclitaxel resistance in breast cancer cell lines (*49*). However, cancers frequently acquire resistance to Bcl-2 inhibitors, a clinically relevant issue in various settings (*22*). Given their effect on increasing cytochrome c release, we hypothesized that Opa1 inhibitors could overcome resistance to Bcl-2 inhibitors in TNBC. We verified whether MYLS22 and Opitor-0 synergized with the Bcl-2 inhibitor ABT-737. Although they expectedly did not directly induce cell death, they significantly enhanced ABT-737 induced apoptosis in a concentration-dependent manner, as demonstrated by the complete rescue of cell death by the pan-caspase inhibitor Z-VAD-FMK. Notably, Opitor-0 was significantly more potent than MYLS22 (Fig. 6G). Zero-potency interaction (ZIP) analysis revealed that the effects of MYLS22 and Opitor-0 were not merely additive but truly synergic with ABT-737. Notably, the δ synergism score of Opitor-0 was fourfold that of MYLS22 and indicative of strong synergism (fig. S7). These findings highlight the potential of Opitor-0 to increase the efficacy of ABT-737 and address the acquired resistance to Bcl-2 inhibitors at least in TNBC.

DISCUSSION

Chemoresistance is a relevant clinical issue in cancer biology. Our study reveals the potential of specific inhibitors of the mitochondrial GTPase Opa1 as a therapeutic strategy to overcome chemoresistance in cancer. By developing small-molecule inhibitors of Opa1 GTPase activity, we uncover a previously unexplored avenue for sensitizing cancer cells to apoptosis. Our findings validate Opa1 as a promising target for cancer therapy and provide a chemical toolbox to dissect its role in mitochondrial dynamics and apoptosis regulation.

Mitochondrial cristae remodeling plays a key role in the regulation of apoptosis that is frequently disrupted in cancer. Opa1 serves as a critical node in this network by maintaining cristae integrity and limiting cytochrome c release (*11*, *42*, *50*, *51*). Notably, mutations that abolish Opa1 GTPase activity also impair its anti-apoptotic function (*11*), suggesting that a selective Opa1 GTPase activity inhibitor could mimic Opa1 down-regulation in a potential anticancer therapy. Through an HTS, we identified MYLS22 as a potent and specific inhibitor of Opa1 GTPase activity. Despite its efficacy, MYLS22 is hindered by limited solubility and moderate potency. By leveraging in silico and in vitro SAR analyses, we developed a handful of second-generation Opitors. Among these compounds, Opitor-0 displays improved potency and pharmacological properties, addressing a key limitation of MYLS22. Our data confirm that inhibiting Opa1 GTPase activity disrupts mitochondrial architecture, leading to cristae remodeling and enhanced cytochrome c release, a prerequisite for caspase activation and apoptosis. These findings extend the role of Opa1 beyond mitochondrial fusion, emphasizing its significance in cancer cell survival.

Developing a specific large dynamin GTPase inhibitor is challenging due to the high degree of homology among the members of

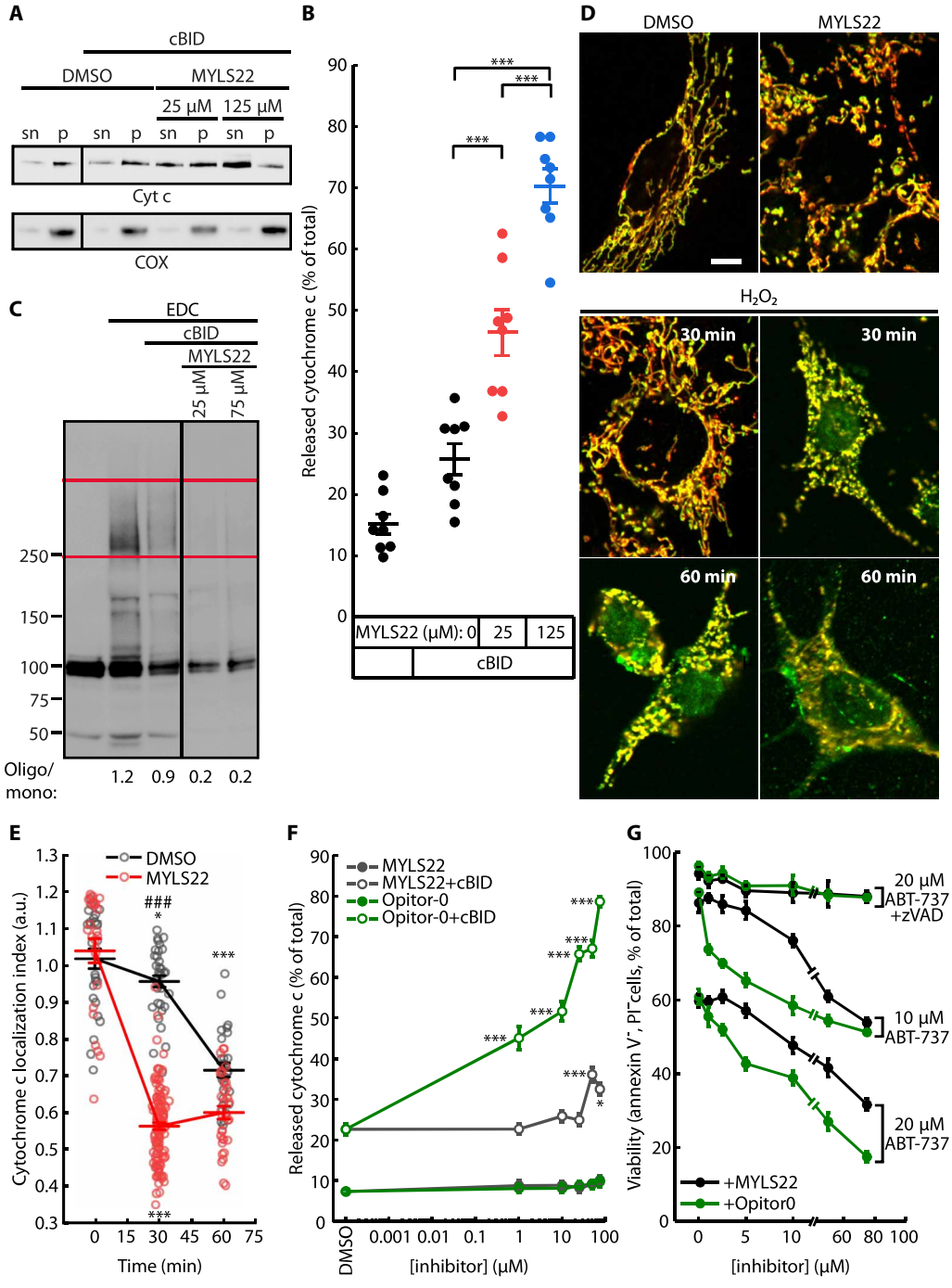

Fig. 6. Opa1 inhibitors enhance apoptotic mitochondrial cytochrome c release and restore breast cancer cell sensitivity to the Bcl-2 inhibitor ABT-737. (**A**) Mouse liver mitochondria incubated for 30 min with cBID (50 pmol/mg) and the indicated concentrations of MYLS22 or DMSO were centrifuged. Equal amounts of protein from pellet (p) and supernatant (sn) were SDS-PAGE separated and immunoblotted as indicated. (**B**) ELISA quantification of cytochrome c release (means ± SEM; $n = 8$ biological replicates) from experiments as in (A). ***$P < 0.0001$ in a one-way ANOVA with Tukey's post hoc test. (**C**) Mouse liver mitochondria treated where indicated for 30 min with cBID (50 pmol/mg) and the indicated concentrations of MYLS22 were cross-linked where indicated with 1 mM EDC, separated by SDS-PAGE and immunoblotted for Opa1. Box highlights Opa1 oligomers. Oligo/mono, OPA1 oligomer/monomer ratio. (**D**) Representative confocal images of MEFs treated with 50 μM MYLS22 and 1 mM H_2O_2 for 0 to 60 min, fixed, and stained for cytochrome c (green) and TOM20 (red). Scale bar, 10 μm. (**E**) Means ± SEM cytochrome c localization index from three to four biological replicates of experiments as in D (25 to 50 cells per condition, dots). Kruskal-Wallis ANOVA versus 0 min: *$P < 0.05$ and ***$P < 0.001$; ###$P < 0.001$, MYLS22 versus DMSO. (**F**) Means ± SEM cytochrome c release by ELISA ($n = 7$ biological replicates) from mitochondria incubated for 30 min with cBID (50 pmol/mg) and the indicated concentrations of MYLS22 or Opitor-0. One-way ANOVA with Tukey's test: *$P < 0.05$ and ***$P < 0.0001$ versus DMSO; $P < 0.0001$ Opitor-0- versus MYLS22-treated mitochondria at each concentration. (**G**) Viability of MDA-MB-231 cells incubated for 12 hours with ABT-737 followed by 5 hours with the indicated concentrations of Opa1 inhibitors ($n = 3$ biological replicates). Where indicated, cells were cotreated with 2 μM pan-caspase inhibitor z-VAD-FMK.

the superfamily (*52*). MYLS22 and Opitor-0 exhibit remarkable specificity, as confirmed by mutational analyses of its binding site on Opa1 and biophysical assays, establishing their utility as chemical probes for Opa1.

Elevated OPA1 expression in various cancers including breast and lung adenocarcinoma, and endometrial cancers (*17*–*19*), correlates with chemoresistance, poor prognosis, and survival (*19*–*21*). In proof-of-concept experiments, down-regulation of Opa1 sensitizes hepatocellular carcinoma and lung cancer cells to cytotoxic treatments and apoptosis (*20*, *53*), the acquisition of resistance toward which represents a major barrier in cancer therapy. The ability of MYLS22 and Opitor-0 to synergize with the Bcl-2 inhibitor ABT-737 is promising. By enhancing cytochrome c release and disrupting a key mechanism of apoptotic resistance at least in TNBC cells, these inhibitors effectively restore sensitivity to Bcl-2 antagonists. Opitor-0, in particular, outperforms MYLS22 in both potency and efficacy, positioning it as a lead candidate for future therapeutic development.

Our findings highlight the therapeutic relevance of mitochondrial dynamics in cancer biology. Beyond their role in overcoming chemoresistance, Opa1 inhibitors offer a platform to explore mitochondrial function in tumorigenesis, metastasis, and therapy response. Although MYLS22 and Opitor-0 represent notable advancements, their translational potential requires further optimization. Challenges such as improving water solubility, and enhancing in vivo pharmacokinetics, by keeping off-target effects minimal, must be addressed.

In conclusion, our study establishes that Opa1 inhibition can facilitate mitochondrial apoptosis and resensitize resistant cancer cells to existing treatments. The development of MYLS22 and its optimized analog Opitor-0 provides not only powerful tools for basic research but also a promising foundation for the design of next-generation cancer therapeutics that can help to address the unmet need for effective strategies against resistant cancers.

MATERIALS AND METHODS

Expression and purification of recombinant proteins

To express recombinant Opa1 (rOpa1) lacking the N-terminal mitochondrial targeting sequence and transmembrane domain, mouse Opa1 transcript variant 2 (NM_133752) was amplified from nucleotide position 502 to the stop codon. For the mini-rOpa1 variant, sequences encoding the G domain and the GED of OPA1 were amplified and linked via a flexible linker, with all cysteine residues mutated to alanine to prevent disulfide bond formation.

The amplified polymerase chain reaction (PCR) products were cloned into the pET21+ vector (Novagen), which adds a C-terminal 6xHis-tag to the encoded proteins. The constructs were transformed into *Escherichia coli* BL21 (DE3) cells for expression. Protein expression was induced with 0.5 μM isopropyl β-D-1-thiogalactopyranoside (IPTG) for 20 hours at 18°C.

Bacterial cells were harvested by centrifugation and resuspended in lysis buffer containing 50 mM tris-HCl, 500 mM NaCl, 10% glycerol, 2 mM $MgCl_2$, 0.5% Triton X-100, 2% Tween 20, and protease inhibitors (cOmplete Ultra EDTA-free, Roche) at pH 8.0. The cells were lysed by sonication on ice, and the lysate was cleared by centrifugation at 14,000*g* for 45 min at 4°C. The supernatant containing the recombinant protein was subjected to Ni^{2+}-NTA affinity chromatography using an FPLC (fast protein liquid chromatography) system (AKTA Pure, GE Healthcare Life Science).

Before elution, the Ni^{2+}-NTA resin was washed with lysis buffer supplemented with 1 mM ATP and 10 mM $MgCl_2$, followed by an additional wash with buffer containing 50 mM tris-HCl, 500 mM NaCl, 10% glycerol, 0.05% Triton X-100, 2 mM $MgCl_2$, and 50 mM imidazole at pH 8.0. The rOpa1 and mini-rOpa1 proteins were eluted using a one-step gradient with elution buffer (50 mM tris-HCl, 500 mM NaCl, 10% glycerol, 0.05% Triton X-100, and 500 mM imidazole at pH 7.4). Imidazole was removed by passage through a HiPrep 26/10 desalting column (GE Healthcare), and the proteins were concentrated using Amicon Ultra centrifugal filters with molecular weight cutoffs of 50 kDa (for full-length rOpa1) and 30 kDa (for mini-rOpa1). Proteins were stored in the storage buffer (50 mM tris-HCl, 150 mM NaCl, 0.05% Triton X-100, and 10% glycerol) at −80°C (*54*).

The T504A and K505N mutant plasmids of mini-rOpa1 were generated using site-directed mutagenesis (QuickChange II Site-Directed Mutagenesis Kit, Agilent) and verified by DNA sequencing. These mutants were expressed and purified following the same protocol as for the full-length rOpa1 and mini-rOpa1.

The recombinant Dynamin-1 protein lacking the PRD (Dyn1ΔPRD) was expressed in *E. coli* and purified as previously described for rOPA1. Protein purity and identity were confirmed via Coomassie staining and Western blot analysis using anti-His and anti-OPA1 primary antibodies, and protein activities were verified and measured with the MG assay.

Recombinant cBID (p7/p15) was expressed, purified, and cleaved with caspase-8 as previously described (*11*).

MG GTPase activity assay

GTPase activity was measured using a modified MG assay, which detects the formation of free phosphate (PO_4) ions resulting from GTP hydrolysis. The phosphate forms a phosphomolybdate complex with ammonium molybdate, which binds to MG dye, causing a measurable absorbance shift at 595 nm (*30*).

The assay was conducted in 96-well plates with a final volume of 190 μl per well. The reaction was initiated by adding 10 μl of 0.5 μM rOpa1 or 1 μM mini-rOpa1 in 50 mM tris-HCl, 150 mM NaCl (pH 7.4) to 10 μl of 500 μM GTP and 10 mM $MgCl_2$. The mixture was incubated at 37°C for 1 hour. The reaction was stopped by adding 5 μl of 500 μM EDTA to chelate Mg^{2+} and prevent further GTP hydrolysis.

For phosphate (P_i) quantification, 150 μl of the MG-ammonium molybdate solution (1 mM MG and 10 mM ammonium molybdate in 1 M HCl) was added to each well. After a 10-min incubation at room temperature, absorbance was measured at 595 nm using a microplate reader. Phosphate concentration was determined from a standard curve (1 to 100 μM P_i) generated for each experiment.

To assess inhibition of rOpa1 or recombinant Dynamin-1 GTPase activity, 5 μl of inhibitor (dissolved in DMSO) or DMSO alone (as solvent control) was preincubated with 0.5 μM rOpa1 or 0.5 μM Dyn1ΔPRD for 20 min at 37°C before initiating the GTP hydrolysis reaction. As a positive control for inhibition, 5 μl of 500 μM EDTA was added before GTP addition. Blank controls contained only buffer and 500 μM GTP (*54*).

High-throughput screening

HTS was conducted using the MyriaScreen Diversity Library II (Sigma-Aldrich, T990000), which comprises 10,000 small molecules selected based on their compliance with Lipinski's Rule of Five,

indicating a high potential for drug-likeness. Each compound in the library was dissolved in DMSO at a concentration of 10 mg/ml. For each round of screening, the compounds were diluted tenfold in 40 mM Hepes/KOH buffer (pH 7.4) and aliquoted into a set of 32 384-well plates. These prepared plates were stored at −20°C until further use. Before conducting the assays, the stock solutions of the compounds were diluted fourfold directly into the assay plates, resulting in final concentrations of 2.5 mg/ml (i.e., ranging from 50 to 200 μM).

The GTPase activity of rOpa1 was assessed using the MG assay. The high-throughput screen was initiated by dispensing 0.5 μM rOpa1 and 5 μl of each compound from the MyriaScreen Diversity Library II, dissolved in 2.5% DMSO, into a total volume of 12 μl per well in a 384-well plate. The process was automated using the Precision XS microplate pipetting system (BioTek). Four columns of the plate were designated for negative controls, where 10% DMSO in 40 mM Hepes/KOH (pH 7.4) was added. For positive inhibition controls, alternating control wells received 5 μl of 0.5 mM EDTA, which inhibits Mg^{2+}-dependent GTP hydrolysis, thereby serving as a control for the inhibition of OPA1 activity. The hydrolysis reaction was initiated after a 10-min incubation at room temperature by adding a solution containing 500 μM GTP and 10 mM $MgCl_2$, resulting in a final reaction volume of 20 μl per well. The plates were then sealed and incubated for 1 hour at 37°C. To terminate the hydrolysis reaction, 5 μl of 0.5 M EDTA was added to each well, except those designated as positive controls. To quantify the phosphate released during the hydrolysis reaction, 60 μl of the MG/ammonium molybdate mixture was added to each well. After a 10-min incubation at room temperature, absorbance was measured at 595 nm using a microplate reader, as previously described (*54*).

The IC_{50} was calculated based on the dose-response curves fitted with a four-parameter logistic curve using OriginPro software.

HTS data analysis

The absorbance data obtained from two replicates of the HTS were analyzed using a customized version of the Bioconductor/R package cellHTS. Initial data processing involved excluding samples with absorbance values lower than the average of the positive control wells (PC), which contained rOpa1 with 1 mM EDTA to fully inhibit GTPase activity. Subsequently, data were normalized on a plate-by-plate basis using the NPI method. For each plate, the average absorbance of the PCs and the negative control wells (NC; containing rOpa1 with DMSO) was calculated. The NPI for each well (NPI_{ki}) was computed using the following formula

$$NPI_{ki} = \frac{x_{ki} - \mu_{PC}}{\mu_{NC} - \mu_{PC}} \tag{1}$$

where x_{ki} represents the raw absorbance value of well k_i, μ_{PC} is the mean absorbance of the positive control wells, and μ_{NC} is the mean absorbance of the negative control wells.

The NPI_{ki} values from each replicate screen were then converted to robust *Z*-scores using the formula

$$\begin{aligned} Robust\ Z_{ki} &= \frac{NPI_{ki} - \widetilde{NPI}}{MAD} \\ MAD &= median\left(|NPI_{ki} - \widetilde{NPI}| \right) \end{aligned} \tag{2}$$

where $\widetilde{NPI}$ is the median, and $|NPI_{ki} - \widetilde{NPI}|$ is the absolute deviations from the median of the NPI values across all plates in a single replicate experiment. The robust Z_{ki} for each compound from the two replicates were averaged, and these average *Z*-scores (Z_{ki}) are plotted in Fig. 1.

As expected, the average *Z*-score for the PCs was 0, whereas the average *Z*-score for the NCs was 1. A Z_{ki} threshold of 0.7 was set to identify potential inhibitors of OPA1 GTPase activity. Compounds with $Z_{ki} \leq 0.7$ in both replicates, as well as in the average of the replicates, were considered hits. Compounds that per se reduced absorbance at the measured wavelength were considered false positives and excluded from further consideration. The SSMD was calculated for each plate to assess assay quality and consistency (*31*)

$$SSMD = \frac{\mu_{NC} - \mu_{PC}}{\sqrt{\sigma_{NC}^2 - \sigma_{PC}^2}} \tag{3}$$

where σ_{NC}^2 and σ_{PC}^2 are the variances of the negative and the positive control wells, respectively.

Molecular modeling and docking studies

The Opa1 protein's coordinates were obtained from the PDB (PDB ID: 6JTG, chain A) (*55*). The structure was prepared using the Structure Preparation tool in MOE 2022. Protonate3D was used to set the appropriate protonation state for titratable residues (pH = 7, T = 310 K, and sal = 0.154). The AMBER10 force field was used to minimize hydrogen atoms until reaching a 0.1 kcal mol^{-1} $Å^{-2}$ gradient. Water molecules, ligands, and buffer components were subsequently removed. The Protein-Ligand ANT System (PLANTS) docking engine with ChemPLP scoring function performed molecular docking (*56*). Each compound generated 10 poses, using a 1.5-Å RMSD (root mean square deviation) threshold to eliminate similar ligand conformations. Docking simulation–derived complexes underwent relaxation through the docking refinement protocol implemented in MOE suite (*57*) using the induced fit option and the GBVI/WSA for the rescoring procedure with default parameters for the energy optimization.

Binding studies by NMR

The NMR experiments were acquired at 298 K on a Bruker 600-MHz spectrometer equipped with an autosampler (64 samples) and a nitrogen-cooled cryoprobe. MYLS22 and Opitor-3 compounds were tested against mini-rOpa1, performing water-ligand observed via STD experiment (*58*) in the presence and absence of the protein. For the more soluble Opitor-3, also, the WaterLOGSY (*59*) experiment was acquired. The protein was buffer exchanged into phosphate-buffered saline (PBS) with a final concentration of 2 μM. The ligands were added at a final concentration of 100 μM (MYLS22) and 200 μM (Opitor-3). Each tube contained 5% (v/v) deuterated water and 4,4-dimethyl-4-silapentane-1-sulfonic acid (DSS) as internal standard (30 μM). For the STD experiments, 48 scans were performed with a mixing time of 2 s. The saturation was pointed at −0.61 and −40 parts per million (ppm) for on-resonance and off-resonance experiments, respectively. In addition, a 25-ms spin-lock was used to eliminate the broad residual protein signal. The WaterLOGSY experiments were conducted using 904 scans, with a 2.5-s recovery delay preceding each scan and a 1.7-s mixing time. These experiments used a 180° inversion pulse applied to the water signal at 4.7 ppm, using a

7.5-ms Gaussian-shaped selective pulse. The NMR spectra were processed and analyzed using Topspin 4.3.1 (Bruker BioSpin GmbH, Rheinstetten, Germany).

SPE of MYLS22

A total of 5×10^5 MEF cells were treated with the indicated concentrations of MYLS22 or DMSO, as a control, in DMEM. After 24 hours, the media were removed, and the cells were washed three times with PBS before being lysed with radioimmunoprecipitation assay buffer. Cell lysates were subjected to protein precipitation: 250 µl of the cell lysate was mixed with 500 µl of a cold acetonitrile (85:15, v/v) solution, vortexed for 2 min, and then centrifuged at 7000*g* for 10 min. The resulting pellet was discarded, and the supernatant was acidified with 2% (v/v) formic acid. In the meanwhile, Strata-X SPE cartridges (Phenomenex, Torrance, CA, USA) were conditioned with 1 ml of methanol, followed by equilibration with 1 ml of water. The acidified supernatants were then loaded onto the cartridges. After washing the cartridges with 10% methanol, the samples were eluted twice with 500 µl of 2% formic acid in acetonitrile. The eluates were analyzed by reversed-phase HPLC. For optimizing the SPE process, aliquots of cell lysates were spiked with MYLS22 and processed similarly.

Reversed-phase HPLC analysis

The SPE samples (20 µl) were injected into a Jupiter C18 chromatographic column (Jupiter C18, 5 µm, 300 Å, 250 mm by 4.6 mm, Phenomenex, Torrance, CA, USA) for analysis. The chromatographic separation was performed at a flow rate of 0.8 ml/min, with a mobile phase consisting of Buffer A [0.1% trifluoroacetic acid (TFA) in bidistilled water] and Buffer B (0.1% TFA in acetonitrile). A gradient elution was applied as follows: 20 to 60% Buffer B over the first 5 min, 60 to 80% Buffer B from 5 to 15 min, and 80 to 100% Buffer B from 15 to 18 min. Between runs, the column was re-equilibrated to the initial mobile phase conditions for ~10 min.

The intracellular amount of MYLS22 was quantified by comparing the area under the curve (AUC) from the HPLC chromatograms of the samples to a calibration curve generated from spiked cell lysate samples. The percentage of intracellular MYLS22 after 5 hours of incubation was determined by relating the amount of the inhibitor extracted from the cell lysates to the initial amount of MYLS22 directly added to the lysates before SPE.

Cell culture

WT and *Opa1*$^{-/-}$ SV40 transformed MEFs (*15*) were cultured in DMEM (Invitrogen) with glucose (4.5 g/liter) supplemented with 10% fetal bovine serum (Invitrogen), 2 mM L-glutamine, penicillin (50 U/ml), streptomycin (50 µg/ml), and 0.1 mM nonessential amino acids (Invitrogen) at 37°C and 5% (v/v) CO_2 in a humidified atmosphere. All cell lines were routinely checked for mycoplasma contamination.

Cell transfection, lentivirus production, and transduction

Cells were transfected using Lipofectamine 3000 (Invitrogen) following the manufacturer's instructions.

Lenti-X 293T cells (Takara Bio) were cotransfected with lentiviral plasmids (pLJM1-Opa1 or pLJM1-Opa1^{K505N}) along with the lentiviral helper psPAX2 and envelope plasmids pCMV-VSV-G using polyethyleneimine (PEI) (PEI MAX MW 40,000, Polysciences). The viral supernatant was collected at 24, 48, and 72 hours post-transfection and used to transduce *Opa1*$^{-/-}$ MEFs in the presence of polybrene (8 µg/ml; Sigma-Aldrich). Twenty-four hours after transduction, the medium was supplemented with puromycin (5 µg/ml; Sigma-Aldrich) to select successfully transduced cells.

Plasmids

Mito-YFP (mtYFP), pMSCV, and pMSCV-Opa1 plasmids were previously described (*9*, *60*). To generate the pMSCV-IRES-mtYFP and pMSCV-Opa1-IRES-mtYFP plasmids, mtYFP and internal ribosomal entry site (IRES) sequences were amplified from the mtYFP and pMSCV-IRES-GFP plasmids, respectively, and cloned into the pMSCV empty vector or the pMSCV-Opa1 vector. The lentiviral plasmids pLJM1-Opa1 was generated by cloning the Opa1 sequence from pMSCV-Opa1 into the pLJM1 empty vector.

The mutant plasmids pLJM1-Opa1^{T504A}, pLJM1-Opa1^{K505N}, pMSCV-Opa1^{T504A}-IRES-mtYFP, and pMSCV-Opa1^{K505N}-IRES-mtYFP were generated via site-directed mutagenesis using the QuickChange II Site-Directed Mutagenesis Kit (Agilent), following the manufacturer's instructions. The primer sequences are reported in Key Resources Table.

Analysis of cell death

MEFs (1×10^5) were grown in 12-well plates and allowed to adhere for 24 hours. Cells were then treated with MYLS22, ABT-737, or DMSO. At specific time points, cells were stained with annexin V–FITC (fluorescein isothiocyanate) and propidium iodide (PI) according to the manufacturer's protocol (eBioscience). Cell viability was assessed by flow cytometry (FACSCalibur, BD Biosciences), as the percentage of cells negative for both annexin V and PI staining.

Imaging of mitochondrial membrane potential with TMRM

To assess mitochondrial membrane potential, MEFs were incubated with 10 nM TMRM (Molecular Probes) in the presence of cyclosporine-H (2 µg/ml) at 37°C for 30 min. Following incubation, sequential images of TMRM fluorescence were captured using the High Content Imaging System Operetta confocal microscope (PerkinElmer) and analyzed with Harmony as previously described (*61*).

Determination of mitochondrial ROS levels

Cells treated as indicated were stained with 2 µM MitoSOX (Invitrogen) in HBSS for 30 min at 37°C in a 5% CO_2 atmosphere. After rinsing with PBS, each sample was split into two tubes: one treated with vehicle and the other with 10 µM AA for 20 min at room temperature. MitoSOX fluorescence was then measured by flow cytometry (FACSCalibur, BD Pharmingen).

Live imaging of the mitochondrial network

To visualize the mitochondrial network, 5×10^4 MEF cells expressing mtYFP were seeded onto 24-mm coverslips and incubated for 5 hours as described. Images were acquired using an Andromeda-iMIC spinning disk confocal microscope (Till Photonics) equipped with ORCA-03G camera (Hamamatsu), a Piezoelectric z-stepper, and a 60X UPLAN 1.35NA oil-immersion objective (Olympus). Stacks of 25 images separated by 0.3 µm along the *z* axis were acquired. Convolution and *z*-stack maximum projections, or three-dimensional (3D) reconstructions with volume rendering in VolumeJ, were performed using ImageJ (National Institutes of Health). Mitochondrial length was quantified with ImageJ by measuring the average major axis length of at least 40 mitochondria per cell in 20 cells per sample (*54*).

Alternatively, MEFs::mtYPF or HeLa::mtYFP cells were seeded in a 384-well plate and treated as detailed, and after 5 hours, imaged

as previously described (*61*) using Operetta-CLS in the confocal mode (PerkinElmer). Image analysis was performed in Harmony (PerkinElmer).

Transmission electron microscopy and morphometric analysis

Cells were fixed for 1 hour at 4°C with freshly prepared 2.5% (v/v) glutaraldehyde in 0.1 M sodium cacodylate (pH 7.4). Fixative was removed, and cells were washed with 0.1 M sodium cacodylate. Cells were postfixed in 1% OsO_4, 1.5% $K_4Fe(CN)_6$ in 0.1 M sodium cacodylate (pH 7.4), stained with 0.5% uranyl acetate, dehydrated in ethanol, and embedded in Embed 812. Thin sections were imaged on a Tecnai G2 (FEI) transmission electron microscope equipped with a Veleta (Olympus Imaging System) digital camera at the Bio-Imaging Facility of the Dept. of Biology, University of Padua. For morphometric analysis, mitochondrial cristae width was measured using the ImageJ Multimeasure plug-in, whereas the number of cristae and cristae junctions were quantified manually.

Mouse liver mitochondria isolation

Mitochondria from mouse liver were purified as previously described (*62*).

Measurement of membrane potential of isolated mitochondria

Membrane potential was assayed by monitoring the fluorescence of Rhodamine 123 (Invitrogen). Mouse liver mitochondria (0.5 mg/ml) were incubated with 0.3 μM Rhodamine 123 and the respiratory substrates 5 mM glutamate/2.5 mM malate or 2 mM succinate in the experimental buffer (EB; 150 mM KCl, 10 mM Tris-Mops, 10 μM EGTA-Tris, 1 mM P_i, and 5 mM glutamate/2.5 mM malate as the respiration substrate, pH 7.4). Following the addition of the inhibitor or vehicle (DMSO), Rhodamine 123 fluorescence was recorded at 25°C, in a microplate reader using $\lambda_{ex} = 485$ nm and $\lambda_{em} = 538$ nm. Measurements were taken before and after the addition of 200 nM uncoupler FCCP (carbonyl cyanide *p*-trifluoromethoxyphenylhydrazone) to fully dissipate the membrane potential.

Mitochondrial cytochrome c release assay

Mouse liver mitochondria (1 mg/ml) were incubated with the inhibitor or vehicle (DMSO) in the presence or absence of recombinant cBID (50 pmol/mg mitochondria) for 15 min at room temperature in EB. Mitochondria were pelleted by centrifugation at 12,000*g* for 10 min at 4°C, and the pellet was resuspended in the same volume of EB. The amount of cytochrome c in the pellet and the supernatant fractions was determined by Western blot using the anti–cytochrome c antibody (BD Pharmingen) or quantified with the Rat/Mouse Cytochrome c Quantikine ELISA (R&D Systems) following the manufacturer's protocol. The percent of released cytochrome c in the supernatant was calculated as: %cytochrome c released = [cytochrome $c_{cytosol}$]/[cytochrome c_{total}] * 100, where cytochrome $c_{cytosol}$ and cytochrome c_{total} represent the amount of cytochrome c detected in the supernatant upon the specific treatment or 2% (v/v) Triton X-100, respectively.

Cytochrome c immunolocalization

For cytochrome c immunolocalization, MEFs were grown on coverslips and treated with the indicated concentration of MYLS22 or DMSO. After 24 hours, cells were treated with 1 mM H_2O_2 to induce apoptosis. After the indicated times, MEFs were fixed and immunostained, as previously described (*63*), with an Alexa Fluor 488–conjugated anti–cytochrome c antibody and an Alexa Fluor 568–conjugated anti-TOM20 antibody. For cytochrome c and TOM20 detection, green and red channel images, respectively, were acquired simultaneously using two separate color channels on the detector assembly of a Zeiss LSM 700 confocal microscope (*54*). The localization index was calculated as previously described (*64*, *65*).

OPA1 protein cross-linking

Mouse liver mitochondria incubated with the recombinant cBID and the indicated concentrations of MYLS22 were cross-linked with the zero-length cross-linker 1-ethyl-3-(3-dimethylaminopropyl)carbodiimide (EDC; Pierce, 10 mM) in PBS for 30 min at 37°C. The reaction was quenched by adding 15 mM dithiothreitol (DTT) for 15 min. Proteins were separated by SDS–polyacrylamide gel electrophoresis (PAGE) and immunoblotted, and Opa1 oligomers were detected with the specific anti-Opa1 antibody (BD Pharmingen).

Cellular thermal shift assay

MEFs were seeded in 10-cm^2 dishes and grown to ~90% confluence. Cells were treated as indicated for 5 hours, harvested by trypsinization, and centrifuged at 500*g* for 5 min. The pellet was washed twice with PBS and resuspended in 1 ml of PBS supplemented with protease inhibitors. Aliquots (100 μl) of cell suspension were transferred into 10 PCR tubes, which were subjected to thermal treatment in a gradient ranging from 37° to 67°C using a thermal cycler for 3 min. After heating, the samples were cooled to room temperature for 3 min. NP-40 was added to each tube to a final concentration of 1% (v/v) to aid in protein solubilization. Cell lysis was achieved through three freeze-thaw cycles, each involving snap-freezing in liquid nitrogen for 1 min followed by thawing at 25°C. The samples were then centrifuged at 20,000*g* for 20 min at 4°C to separate soluble protein fractions from precipitates. Equal volumes of the supernatants were subjected to SDS-PAGE and analyzed via Western blotting. Actin, a temperature-insensitive protein, was used as a loading control. The relative intensities of the protein bands were normalized to the intensity at the lowest temperature (37°C) and plotted against the corresponding heating temperatures. The data were fitted using a nonlinear regression curve to calculate the apparent melting temperature (T_m). The T_m values of OPA1 with and without the compound were compared.

Calculation of combination synergy factor

Synergism between MYLS22 and ABT-737 or Opitor-0 and ABT-737 was quantified with SynergyFinder supplied as an R package (https://bioconductor.org/packages/release/bioc/html/synergyfinder.html). Synergy score based on the ZIP model is visualized as a 2D landscape dose-response matrix. The overall levels of synergy effects of the two compounds are shown as delta score.

Statistical analysis

Statistical analysis was performed using OriginPro 9.0 (Microcal). Normal distribution of populations at the 0.001 level was calculated using the Shapiro-Wilk normality test. Homogeneity of variance was calculated with Levene's test. Parametric statistical significance was determined using one-way analysis of variance (ANOVA); if nonparametric, Kruskal-Wallis ANOVA was used. *P* values are indicated in the figure legends.

Supplementary Materials

The PDF file includes:

Supplementary Text
Figs. S1 to S7
Tables S1 to S3
Legends for movies S1 and S2
Legends for datasets S1 and S2
References

Other Supplementary Material for this manuscript includes the following:

Movies S1 and S2
Datasets S1 and S2

REFERENCES AND NOTES

1. A. Kasahara, L. Scorrano, Mitochondria: From cell death executioners to regulators of cell differentiation. *Trends Cell Biol.* **24**, 761–770 (2014).
2. D. Hanahan, R. A. Weinberg, Hallmarks of cancer: The next generation. *Cell* **144**, 646–674 (2011).
3. A. Kasahara, S. Cipolat, Y. Chen, G. W. Dorn, L. Scorrano, Mitochondrial fusion directs cardiomyocyte differentiation via calcineurin and Notch signaling. *Science* **342**, 734–737 (2013).
4. L. C. Gomes, B. G. Di, L. Scorrano, During autophagy mitochondria elongate, are spared from degradation and sustain cell viability. *Nat. Cell Biol.* **13**, 589–598 (2011).
5. M. Sciacovelli, E. Goncalves, T. I. Johnson, V. R. Zecchini, A. S. da Costa, E. Gaude, A. V. Drubbel, S. J. Theobald, S. R. Abbo, M. G. Tran, V. Rajeeve, S. Cardaci, S. Foster, H. Yun, P. Cutillas, A. Warren, V. Gnanapragasam, E. Gottlieb, K. Franze, B. Huntly, E. R. Maher, P. H. Maxwell, J. Saez-Rodriguez, C. Frezza, Fumarate is an epigenetic modifier that elicits epithelial-to-mesenchymal transition. *Nature* **537**, 544–547 (2016).
6. S. Campello, R. A. Lacalle, M. Bettella, S. Manes, L. Scorrano, A. Viola, Orchestration of lymphocyte chemotaxis by mitochondrial dynamics. *J. Exp. Med.* **203**, 2879–2886 (2006).
7. L. Pernas, L. Scorrano, Mito-morphosis: Mitochondrial fusion, fission, and cristae remodeling as key mediators of cellular function. *Annu. Rev. Physiol.* **78**, 505–531 (2016).
8. B. Zhivotovsky, S. Orrenius, O. T. Brustugun, S. O. Doskeland, Injected cytochrome c induces apoptosis. *Nature* **391**, 449–450 (1998).
9. S. Cipolat, O. Martins. de Brito, B. Dal Zilio, L. Scorrano, OPA1 requires mitofusin 1 to promote mitochondrial fusion. *Proc. Natl. Acad. Sci. U.S.A.* **101**, 15927–15932 (2004).
10. S. Cogliati, J. A. Enriquez, L. Scorrano, Mitochondrial cristae: Where beauty meets functionality. *Trends Biochem. Sci.* **41**, 261–273 (2016).
11. C. Frezza, S. Cipolat, O. Martins. de Brito, M. Micaroni, G. V. Beznoussenko, T. Rudka, D. Bartoli, R. S. Polishuck, N. N. Danial, B. De Strooper, L. Scorrano, OPA1 controls apoptotic cristae remodeling independently from mitochondrial fusion. *Cell* **126**, 177–189 (2006).
12. R. Yamaguchi, L. Lartigue, G. Perkins, R. T. Scott, A. Dixit, Y. Kushnareva, T. Kuwana, M. H. Ellisman, D. D. Newmeyer, Opa1-mediated cristae opening is Bax/Bak and BH3 dependent, required for apoptosis, and independent of Bak oligomerization. *Mol. Cell* **31**, 557–569 (2008).
13. T. Landes, L. J. Emorine, D. Courilleau, M. Rojo, P. Belenguer, L. Arnaune-Pelloquin, The BH3-only Bnip3 binds to the dynamin Opa1 to promote mitochondrial fragmentation and apoptosis by distinct mechanisms. *EMBO Rep.* **11**, 459–465 (2010).
14. L. Scorrano, M. Ashiya, K. Buttle, S. Weiler, S. A. Oakes, C. A. Mannella, S. J. Korsmeyer, A distinct pathway remodels mitochondrial cristae and mobilizes cytochrome c during apoptosis. *Dev. Cell* **2**, 55–67 (2002).
15. S. Cogliati, C. Frezza, M. E. Soriano, T. Varanita, R. Quintana-Cabrera, M. Corrado, S. Cipolat, V. Costa, A. Casarin, L. C. Gomes, E. Perales-Clemente, L. Salviati, P. Fernandez-Silva, J. A. Enriquez, L. Scorrano, Mitochondrial cristae shape determines respiratory chain supercomplexes assembly and respiratory efficiency. *Cell* **155**, 160–171 (2013).
16. J. Qian, P. P. Massion, Role of chromosome 3q amplification in lung cancer. *J. Thorac. Oncol.* **3**, 212–215 (2008).
17. G. R. Anderson, S. E. Wardell, M. Cakir, C. Yip, Y.-R. Ahn, M. Ali, A. P. Yllanes, C. A. Chao, D. P. McDonnell, K. C. Wood, Dysregulation of mitochondrial dynamics proteins are a targetable feature of human tumors. *Nat. Commun.* **9**, 1677 (2018).
18. Y. Wee, Y. Liu, J. Lu, X. Li, M. Zhao, Identification of novel prognosis-related genes associated with cancer using integrative network analysis. *Sci. Rep.* **8**, 3233 (2018).
19. H. Y. Fang, C. Y. Chen, S. H. Chiou, Y. T. Wang, T. Y. Lin, H. W. Chang, I. P. Chiang, K. J. Lan, K. C. Chow, Overexpression of optic atrophy 1 protein increases cisplatin resistance via inactivation of caspase-dependent apoptosis in lung adenocarcinoma cells. *Hum. Pathol.* **43**, 105–114 (2012).
20. X. Zhao, C. Tian, W. M. Puszyk, O. O. Ogunwobi, M. Cao, T. Wang, R. Cabrera, D. R. Nelson, C. Liu, OPA1 downregulation is involved in sorafenib-induced apoptosis in hepatocellular carcinoma. *Lab. Invest.* **93**, 8–19 (2013).
21. B. Kong, Q. Wang, E. Fung, K. Xue, B. K. Tsang, p53 is required for cisplatin-induced processing of the mitochondrial fusion protein L-Opa1 that is mediated by the mitochondrial metallopeptidase Oma1 in gynecologic cancers. *J. Biol. Chem.* **289**, 27134–27145 (2014).
22. X. Chen, C. Glytsou, H. Zhou, S. Narang, D. E. Reyna, A. Lopez, T. Sakellaropoulos, Y. Gong, A. Kloetgen, Y. S. Yap, E. Wang, E. Gavathiotis, A. Tsirigos, R. Tibes, I. Aifantis, Targeting mitochondrial structure sensitizes acute myeloid leukemia to venetoclax treatment. *Cancer Discov.* **9**, 890–909 (2019).
23. S. Herkenne, O. Ek, M. Zamberlan, A. Pellattiero, M. Chergova, I. Chivite, E. Novotná, G. Rigoni, T. B. Fonseca, D. Samardzic, A. Agnellini, C. Bean, G. Di Benedetto, N. Tiso, F. Argenton, A. Viola, M. E. Soriano, M. Giacomello, E. Ziviani, G. Sales, M. Claret, M. Graupera, L. Scorrano, Developmental and tumor angiogenesis requires the mitochondria-shaping protein Opa1. *Cell Metab.* **31**, 987–1003.e1008 (2020).
24. M. Zamberlan, A. Boeckx, F. Muller, F. Vinelli, O. Ek, C. Vianello, E. Coart, K. Shibata, A. Christian, F. Grespi, M. Giacomello, I. Struman, L. Scorrano, S. Herkenne, Inhibition of the mitochondrial protein Opa1 curtails breast cancer growth. *J. Exp. Clin. Cancer Res.* **41**, 95 (2022).
25. M. L. Baek, J. Lee, K. E. Pendleton, M. J. Berner, E. B. Goff, L. Tan, S. A. Martinez, I. Mahmud, T. Wang, M. D. Meyer, B. Lim, J. P. Barrish, W. Porter, P. L. Lorenzi, G. V. Echeverria, Mitochondrial structure and function adaptation in residual triple negative breast cancer cells surviving chemotherapy treatment. *Oncogene* **42**, 1117–1131 (2023).
26. M. Noguchi, S. Kohno, A. Pellattiero, Y. Machida, K. Shibata, N. Shintani, T. Kohno, N. Gotoh, C. Takahashi, A. Hirao, L. Scorrano, A. Kasahara, Inhibition of the mitochondria-shaping protein Opa1 restores sensitivity to Gefitinib in a lung adenocarcinomaresistant cell line. *Cell Death Dis.* **14**, 241 (2023).
27. C. Larrue, S. Mouche, S. Lin, F. Simonetta, N. K. Scheidegger, L. Poulain, R. Birsen, J. E. Sarry, K. Stegmaier, J. Tamburini, Mitochondrial fusion is a therapeutic vulnerability of acute myeloid leukemia. *Leukemia* **37**, 765–775 (2023).
28. R. Quintana-Cabrera, C. Quirin, C. Glytsou, M. Corrado, A. Urbani, A. Pellattiero, E. Calvo, J. Vázquez, J. A. Enríquez, C. Gerle, M. E. Soriano, P. Bernardi, L. Scorrano, The cristae modulator Optic atrophy 1 requires mitochondrial ATP synthase oligomers to safeguard mitochondrial function. *Nat. Commun.* **9**, 3399 (2018).
29. A. Cassidy-Stone, J. E. Chipuk, E. Ingerman, C. Song, C. Yoo, T. Kuwana, M. J. Kurth, J. T. Shaw, J. E. Hinshaw, D. R. Green, J. Nunnari, Chemical inhibition of the mitochondrial division dynamin reveals its role in Bax/Bak-dependent mitochondrial outer membrane permeabilization. *Dev. Cell* **14**, 193–204 (2008).
30. M. Leonard, B. Doo Song, R. Ramachandran, S. L. Schmid, "Robust colorimetric assays for dynamin's basal and stimulated GTPase activities" in *Methods in Enzymology* (Academic Press, 2005), vol. 404, pp. 490–503.
31. X. D. Zhang, A pair of new statistical parameters for quality control in RNA interference high-throughput screening assays. *Genomics* **89**, 552–561 (2007).
32. K. B. Teuscher, M. Zhang, H. Ji, A versatile method to determine the cellular bioavailability of small-molecule inhibitors. *J. Med. Chem.* **60**, 157–169 (2017).
33. C. A. Lipinski, F. Lombardo, B. W. Dominy, P. J. Feeney, Experimental and computational approaches to estimate solubility and permeability in drug discovery and development settings. *Adv. Drug Deliv. Rev.* **46**, 3–26 (2001).
34. W. A. Irwin, N. Bergamin, P. Sabatelli, C. Reggiani, A. Megighian, L. Merlini, P. Braghetta, M. Columbaro, D. Volpin, G. M. Bressan, P. Bernardi, P. Bonaldo, Mitochondrial dysfunction and apoptosis in myopathic mice with collagen VI deficiency. *Nat. Genet.* **35**, 367–371 (2003).
35. H. Chen, A. Chomyn, D. C. Chan, Disruption of fusion results in mitochondrial heterogeneity and dysfunction. *J. Biol. Chem.* **280**, 26185–26192 (2005).
36. Z. Song, H. Chen, M. Fiket, C. Alexander, D. C. Chan, OPA1 processing controls mitochondrial fusion and is regulated by mRNA splicing, membrane potential, and Yme1L. *J. Cell Biol.* **178**, 749–755 (2007).
37. T. Ban, T. Ishihara, H. Kohno, S. Saita, A. Ichimura, K. Maenaka, T. Oka, K. Mihara, N. Ishihara, Molecular basis of selective mitochondrial fusion by heterotypic action between OPA1 and cardiolipin. *Nat. Cell Biol.* **19**, 856–863 (2017).
38. H. Lee, S. B. Smith, Y. Yoon, The short variant of the mitochondrial dynamin OPA1 maintains mitochondrial energetics and cristae structure. *J. Biol. Chem.* **292**, 7115–7130 (2017).
39. D. M. Molina, R. Jafari, M. Ignatushchenko, T. Seki, E. A. Larsson, C. Dan, L. Sreekumar, Y. Cao, P. Nordlund, Monitoring drug target engagement in cells and tissues using the cellular thermal shift assay. *Science* **341**, 84–87 (2013).
40. R. Jafari, H. Almqvist, H. Axelsson, M. Ignatushchenko, T. Lundbäck, P. Nordlund, D. M. Molina, The cellular thermal shift assay for evaluating drug target interactions in cells. *Nat. Protoc.* **9**, 2100–2122 (2014).
41. F. B. M. Reinhard, D. Eberhard, T. Werner, H. Franken, D. Childs, C. Doce, M. F. Savitski, W. Huber, M. Bantscheff, M. M. Savitski, G. Drewes, Thermal proteome profiling monitors ligand interactions with cellular membrane proteins. *Nat. Methods* **12**, 1129–1131 (2015).

42. A. Olichon, L. Baricault, N. Gas, E. Guillou, A. Valette, P. Belenguer, G. Lenaers, Loss of OPA1 perturbates the mitochondrial inner membrane structure and integrity, leading to cytochrome c release and apoptosis. *J. Biol. Chem.* **278**, 7743–7746 (2003).
43. Y. J. Lee, S. Y. Jeong, M. Karbowski, C. L. Smith, R. J. Youle, Roles of the mammalian mitochondrial fission and fusion mediators Fis1, Drp1, and Opa1 in apoptosis. *Mol. Biol. Cell* **15**, 5001–5011 (2004).
44. A. Olichon, T. Landes, L. Arnaune-Pelloquin, L. J. Emorine, V. Mils, A. Guichet, C. Delettre, C. Hamel, P. Amati-Bonneau, D. Bonneau, P. Reynier, G. Lenaers, P. Belenguer, Effects of OPA1 mutations on mitochondrial morphology and apoptosis: Relevance to ADOA pathogenesis. *J. Cell Physiol.* **211**, 423–430 (2007).
45. L. Scorrano, S. A. Oakes, J. T. Opferman, E. H. Cheng, M. D. Sorcinelli, T. Pozzan, S. J. Korsmeyer, BAX and BAK regulation of endoplasmic reticulum Ca^{2+}: A control point for apoptosis. *Science* **300**, 135–139 (2003).
46. C. Liedtke, C. Mazouni, K. R. Hess, F. Andre, A. Tordai, J. A. Mejia, W. F. Symmans, A. M. Gonzalez-Angulo, B. Hennessy, M. Green, M. Cristofanilli, G. N. Hortobagyi, L. Pusztai, Response to neoadjuvant therapy and long-term survival in patients with triple-negative breast cancer. *J. Clin. Oncol.* **26**, 1275–1281 (2008).
47. L. M. High, B. Szymanska, U. Wilczynska-Kalak, N. Barber, R. O'Brien, S. L. Khaw, I. B. Vikstrom, A. W. Roberts, R. B. Lock, The Bcl-2 homology domain 3 mimetic ABT-737 targets the apoptotic machinery in acute lymphoblastic leukemia resulting in synergistic in vitro and in vivo interactions with established drugs. *Mol. Pharmacol.* **77**, 483–494 (2010).
48. J. Kuroda, S. Kimura, M. Andreeff, E. Ashihara, Y. Kamitsuji, A. Yokota, E. Kawata, M. Takeuchi, R. Tanaka, Y. Murotani, Y. Matsumoto, H. Tanaka, A. Strasser, M. Taniwaki, T. Maekawa, ABT-737 is a useful component of combinatory chemotherapies for chronic myeloid leukaemias with diverse drug-resistance mechanisms. *Br. J. Haematol.* **140**, 181–190 (2008).
49. O. Kutuk, A. Letai, Alteration of the mitochondrial apoptotic pathway is key to acquired paclitaxel resistance and can be reversed by ABT-737. *Cancer Res.* **68**, 7985–7994 (2008).
50. L. Griparic, N. N. van der Wel, I. J. Orozco, P. J. Peters, A. M. van der Bliek, Loss of the intermembrane space protein Mgm1/OPA1 induces swelling and localized constrictions along the lengths of mitochondria. *J. Biol. Chem.* **279**, 18792–18798 (2004).
51. V. Del Dotto, P. Mishra, S. Vidoni, M. Fogazza, A. Maresca, L. Caporali, J. M. McCaffery, M. Cappelletti, E. Baruffini, G. Lenaers, D. Chan, M. Rugolo, V. Carelli, C. Zanna, OPA1 isoforms in the hierarchical organization of mitochondrial functions. *Cell Rep.* **19**, 2557–2571 (2017).
52. E. A. Bordt, P. Clerc, B. A. Roelofs, A. J. Saladino, L. Tretter, V. Adam-Vizi, E. Cherok, A. Khalil, N. Yadava, S. X. Ge, T. C. Francis, N. W. Kennedy, L. K. Picton, T. Kumar, S. Uppuluri, A. M. Miller, K. Itoh, M. Karbowski, H. Sesaki, R. B. Hill, B. M. Polster, The putative Drp1 inhibitor mdivi-1 is a reversible mitochondrial complex I inhibitor that modulates reactive oxygen species: Developmental cell. *Dev. Cell* **40**, 583–594.e6 (2017).
53. S. K. Hwang, A. Minai-Tehrani, K. N. Yu, S. H. Chang, J. E. Kim, K. H. Lee, J. Park, G. R. Beck, M. H. Cho, Carboxyl-terminal modulator protein induces apoptosis by regulating mitochondrial function in lung cancer cells. *Int. J. Oncol.* **40**, 1515–1524 (2012).
54. A. Pellattiero, "Pharmacological modulation of mitochondrial dynamics: Identification of a specific OPA1 inhibitor to enhance apoptotic release of cytochrome c," thesis, University of Padova, Padova (2019).
55. C. Yu, J. Zhao, L. Yan, Y. Qi, X. Guo, Z. Lou, J. Hu, Z. Rao, Structural insights into G domain dimerization and pathogenic mutation of OPA1. *J. Cell Biol.* **219**, e201907098 (2020).
56. O. Korb, T. Stützle, T. E. Exner, paper presented at the *Proceedings of the 5th international conference on Ant Colony Optimization and Swarm Intelligence*, Brussels, Belgium, 2006.
57. Chemical Computing Group (CCG), MOE suite (CCG, 2025).
58. M. Mayer, B. Meyer, Characterization of ligand binding by saturation transfer difference NMR spectroscopy. *Angew. Chem. Int. Ed. Engl.* **38**, 1784–1788 (1999).
59. C. Dalvit, P. Pevarello, M. Tatò, M. Veronesi, A. Vulpetti, M. Sundström, Identification of compounds with binding affinity to proteins via magnetization transfer from bulk water. *J. Biomol. NMR* **18**, 65–68 (2000).
60. M. Zaninello, K. Palikaras, D. Naon, K. Iwata, S. Herkenne, R. Quintana-Cabrera, M. Semenzato, F. Grespi, F. N. Ross-Cisneros, V. Carelli, A. A. Sadun, N. Tavernarakis, L. Scorrano, Inhibition of autophagy curtails visual loss in a model of autosomal dominant optic atrophy. *Nat. Commun.* **11**, 4029 (2020).
61. C. Vianello, F. Dal Bello, S. H. Shin, S. Schiavon, C. Bean, A. P. Magalhães Rebelo, T. Knedlík, E. N. Esfahani, V. Costiniti, R. S. Lacruz, G. Covello, F. Munari, T. Scolaro, A. Viola, E. Rampazzo, L. Persano, S. Zumerle, L. Scorrano, A. Gianelle, M. Giacomello, High-throughput microscopy analysis of mitochondrial membrane potential in 2D and 3D models. *Cells* **12**, 1089 (2023).
62. C. Frezza, S. Cipolat, L. Scorrano, Organelle isolation: Functional mitochondria from mouse liver, muscle and cultured fibroblasts. *Nat. Protoc.* **2**, 287–295 (2007).
63. L. Scorrano, S. J. Korsmeyer, Mechanisms of cytochrome c release by proapoptotic BCL-2 family members. *Biochem. Biophys. Res. Commun.* **304**, 437–444 (2003).
64. C. Frezza, S. Cipolat, L. Scorrano, Measuring mitochondrial shape changes and their consequences on mitochondrial involvement during apoptosis. *Methods Mol. Biol.* **372**, 405–420 (2007).
65. V. Petronilli, D. Penzo, L. Scorrano, P. Bernardi, F. Di Lisa, The mitochondrial permeability transition, release of cytochrome c and cell death. Correlation with the duration of pore openings in situ. *J. Biol. Chem.* **276**, 12030–12034 (2001).
66. A. Quan, P. J. Robinson, Rapid purification of native dynamin I and colorimetric GTPase assay. *Methods Enzymol.* **404**, 556–569 (2005).

Acknowledgments: MMS Lab is grateful to the Chemical Computing Group for scientific and technical partnership. We thank F. Caicci, E. Boldrin, G. Covello, and S. Schiavon (DiBioImaging Facility) for EM sample preparation and analysis and for help with high-content imaging. **Funding:** This work was supported by the AIRC IG15748 (L.S.); AIRC IG19991 (L.S.); AIRC IG27307 (L.S.); European Research Council (ERC) FP7-282280 (L.S.); European Union FP7 CIG PCIG13-GA-2013-618697 (L.S.); MIUR FIRB RBAP11Z3YA_005 (L.S.); MIUR PRIN 2017BF3PXZ (L.S.); MUR PRIN P2022JZ9RE_002 (L.S.); European Union Next Generation EU, Mission 4 Component 2 B73C22001250006 (L.S.); Fondazione Cariparo doctoral fellowship (C.Q.); FP7-Cofund DTI-IMPORT (S.H.); AIRC Postdoctoral Fellowship (SH); University of Liège Fonds Léon Frédéricq (S.H.); Foundation Umberto Veronesi fellowship (S.H.); and AIRC 3-year Fellowship (A.P.). **Author contributions:** Conceptualization: A.M., L.C., L.S., C.Q., and A.P. Data curation: L.S., C.Q., S.M., and A.P. Formal analysis: L.S., C.Q., S.M., S.H., F.M., A.P., and N.B. Funding acquisition: L.S. Investigation: A.M., L.C., M.S., C.Q., S.M., A.F., S.H., F.M., E.G., A.P., and N.B. Methodology: A.M., L.C., M.S., L.S., C.Q., F.M., A.P., and N.B. Project administration: L.S. Resources: A.M., L.C., and N.B. Software: C.Q. and S.M. Supervision: A.M., L.C., L.S., S.M., and E.G. Validation: L.C., C.Q., S.M., S.H., F.M., and A.P. Visualization: L.C., M.S., L.S., C.Q., S.M., E.G., A.P., and N.B. Writing—original draft: A.M., L.S., C.Q., S.M., A.P., and N.B. Writing—review and editing: A.M., L.C., L.S., C.Q., S.M., E.G., A.P., and N.B. **Competing interests:** L.S., A.P., and C.Q. disclose that they are inventors of a submitted patent application by the University of Padova and Veneto Institute of Molecular Medicine covering MYLS22 and its derivatives as Opa1 inhibitors (WIPO|PCT WO2021/008669). The other authors declare that they have no competing interests. **Data and materials availability:** All data needed to evaluate the conclusions in the paper are present in the paper and/or the Supplementary Materials. Raw data from the HTS are available as dataset S1. Raw data used for generation of graphs and uncropped Western blots are available as dataset S2.

Submitted 16 March 2025
Accepted 30 May 2025
Published 4 July 2025
10.1126/sciadv.adx4562